E-789

NORTHERN ILLINOIS UNIVERSITY

SCALER ANALYSIS PERFORMED FOR THE STUDY OF THE NUCLEAR DEPENDENCE OF J/ψ PRODUCTION AT FEYNMAN-x NEAR ZERO

A THESIS SUBMITTED TO THE GRADUATE SCHOOL
IN PARTIAL FULFILLMENT OF THE REQUIREMENTS
FOR THE DEGREE
MASTER OF SCIENCE

DEPARTMENT OF PHYSICS

BY
VICTORIA MARTIN-CASTILLA

DEKALB, ILLINOIS
AUGUST 1995

Certification: In accordance with departmental and Graduate School policies, this thesis is accepted in partial fulfillment of degree requirements.

Thesis Director

Date

ABSTRACT

Name: Victoria Martin-Castilla Department: Physics

Title: Scaler Analysis Performed for the Study of the Nuclear Dependence of J/ψ Production at Feynman-x Near Zero

Major: Physics Degree: Master of Science

Approved by: Date:

Daniel Cole 7/17/95

Thesis Director

NORTHERN ILLINOIS UNIVERSITY

ABSTRACT

This thesis describes the data analysis on beam and apparatus monitors of an experiment performed as part of Fermilab E789. The experiment studied the nuclear dependence of J/ψ production at values of the longitudinal momentum fraction, x_F (Feynman-x), from -0.1 to $+0.1$. J/ψ resonances were produced by an 800 GeV proton beam incident on beryllium, carbon, and tungsten targets. J/ψs were detected in the $\mu^+\mu^-$ decay channel.

ACKNOWLEDGEMENTS

Completing this thesis has been a big relief to me. Four years ago, when I started, I did not anticipate it would take me this long, nor it would be such a learning experience. At the end of this achievement, I would like to recognize those who in various ways helped and encouraged me to keep up with this work.

First of all, I want to thank my thesis advisor, professor Daniel Kaplan. Without his guidance and careful reading of the various versions of this thesis, this work would never have been as good as it is now. I am greatly in debt to him for all I have learned while working on the experiment and writing this thesis. I sincerely appreciate his advice through a personal problem.

I want also to recognize the hard work done by all members of the experiment E789. It was a great experience to be part of this group. In particular, I want to thank Mike Leitch for his explanations of the data analysis process and his initial assistance with the scaler analysis. I want to thank Chuck Brown for his inputs on the behavior of the data. I must also thank Derek Lane for creating the n-tuple file that I have been using in the scaler analysis.

I would like to thank my committee members Daniel Kaplan, Dave Hedin, and John Shaffer for reading the thesis and for their comments.

I greatly appreciate professor Bernard Pope for his encouragement and

understanding. I thank professor Raymond Brock for his insistence on my finishing this thesis.

I am grateful to my friends for their unconditional friendship.

I want to thank my parents, brothers, and sisters for their love, understanding, unselfishness, and encouragement. I thank my parents for being my constant support. They are always a model for me.

To my parents, brothers and sisters, and in the memory of my older brother who recently passed away.

TABLE OF CONTENTS

Page

Appendix

LIST OF TABLES

LIST OF FIGURES

Page

Chapter 1
INTRODUCTION

This thesis describes the scaler[1] analysis performed on apparatus and beam monitors to study the nuclear dependence of J/ψ production at values of longitudinal momentum fraction, Feynman-x (x_F), from -0.1 to $+0.1$, extending such measurements to negative values of x_F, where no experimental data were previously available. The J/ψs were produced by an 800-GeV proton beam incident on beryllium, carbon, and tungsten targets. They were detected in the $\mu^+\mu^-$ decay channel. The data were taken by the E789 collaboration at Fermilab's Meson East laboratory during part of the summer of 1990. Although the main purpose of E789 was the study of charmless two-body decays of neutral b-quark hadrons [1], during the fixed-target run of 1990 the group decided to study dileptonic decays of charmonium and two-body decays of neutral D mesons.[2] The charmonium work enabled us to broaden the Feynman-x range of measurements of the nuclear dependence of J/ψ while tuning up the apparatus and debugging the new and modified elements of the spectrometer in preparation for the beauty running.

The dependence of the production of the J/ψ resonance in proton-nucleus collisions on the species of the target nucleus has become a subject of con-

[1] Scalers are introduced in Chapter 4.

[2] A D meson is a combination of a charm quark with an up or down antiquark.

siderable interest in light of recent results on the nuclear dependence of other processes. To put these matters into proper perspective, we first consider the internal structure of nucleons.

1.1 Hadron Constituents

First theoretically [2] and later experimentally [3], it has been proved that strongly interacting particles (hadrons) such as nucleons, π mesons, etc., are made up of apparently point-like constituents. These constituents (quarks, antiquarks, and gluons) are collectively called partons. As far as we know, quarks are the fundamental constituents of matter. They have spin $\frac{1}{2}$ and non-integral charge. Gluons, on the other hand, are the quantum of interaction of the strong force[3]. They are electrically neutral with spin 1. Quarks are found only in combinations of three quarks and quark-antiquark. These combinations are called baryon and meson, respectively. Other combinations of quarks and antiquarks have not been observed.

The J/ψ-meson, the particle studied in this experiment, is a charm-anticharm bound state with a mass of 3.097 GeV and a lifetime of 10^{-20}sec. It was discovered independently at Brookhaven by Ting's group [4] and at SLAC by Richter's group [5] in 1974 in proton-nucleon collisions and electron-positron annihilation respectively. The importance of the discovery of this particle was the appearance of the charm quark, a new flavor[4] introduced theoretically

[3]The force responsible for holding protons and neutrons together in the nucleus.

[4]At that time the flavors known were up, down, and strange. The beauty quark was added to the list later on. The last flavor, the top quark, although predicted by the theory, was not discovered until recently. Theoretical predictions postulate the existence of another

first by Bjorken and Glashow [6] in 1964 and later by Glashow, Iliopoulos, and Maiani [7] in 1970. The appearance of this new quark was a confirmation that the theoretical model of the elementary constituents of matter was on the right track. It also restored the parallelism between families or generations in quarks and leptons, a parallelism that has been confirmed at Fermilab with the recent discovery of the top quark [8] in March 1995.

1.2 The Parton Structure Functions of Nucleons

Hadron constituents (partons) each carry a fraction of the total hadron longitudinal momentum. The probability distribution of finding a parton with a certain fraction x of the total longitudinal momentum is given by the so-called structure functions. Structure functions of partons within nucleons have been measured mostly by deep-inelastic lepton (e^-, μ^-, ν) scattering from nucleons (Fig. 1.1).[5] Neglecting the nuclear binding energies (since nuclear binding energies per nucleon are around 8 MeV, and typical energy transfers in deep-inelastic lepton scattering are of the order of GeV [9]), it was originally assumed that deep-inelastic scattering on a nucleus of atomic number A was just an incoherent sum of scattering on A nucleons. In 1983 however, the European Muon Collaboration [10], comparing the deep-inelastic scattering of muons from deuterium[6] and iron, found that the nucleon structure function is modi-

quark called top. The top quark was finally discovered at Fermilab in March 1995.

[5] In deep-inelastic scattering a lepton interacts via a virtual photon with a charged parton (quark) inside a nucleon giving a lepton plus hadrons.

[6] The deuteron is a loosely bound system and therefore the two nucleons that form it are essentially free nucleons.

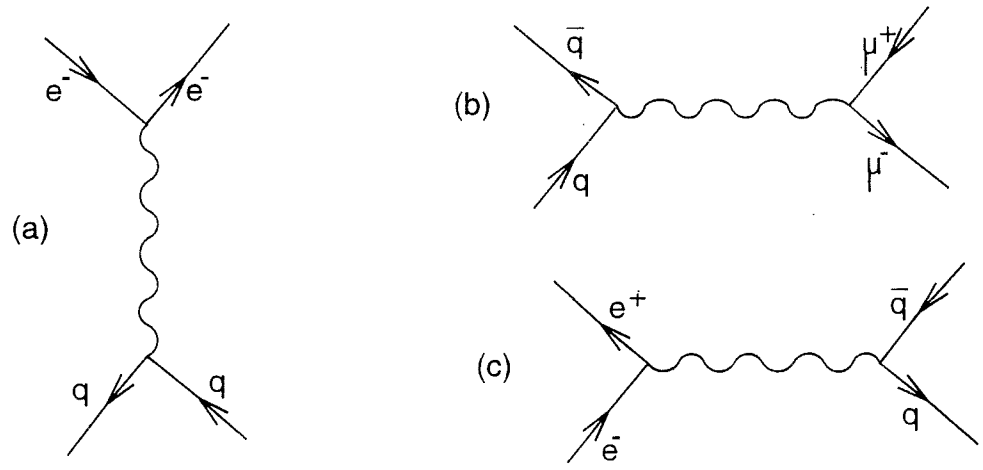

Figure 1.1: Feynman diagrams for various processes of interest. (a) deep inelastic lepton scattering, (b) Drell-Yan process, and (c) electron-positron annihilation.

fied by the nuclear environment. This result has so far resisted explanation in Quantum Chromodynamics (QCD).[7]

If quark structure functions are modified in nuclei, gluon structure functions might be modified as well. To study the structure functions of gluons one needs an appropriate probe. Deep-inelastic lepton scattering is insensitive to gluon structure functions because gluons interact only strongly. Lepto-, photo-, and hadroproduction of heavy mesons such as J/ψ, Υ, etc., as well as direct production of high transverse-momentum photons, are sensitive to gluon distributions [11].

In E789, J/ψs were created by hadroproduction, in which a proton from

[7]The theory that seeks to explain the interactions of gluons and quarks, that is, the theory of the strong interaction.

the beam interacts with a nucleon in the target producing J/ψ plus hadrons:

$$p + A \rightarrow J/\psi + \text{anything}.$$

Therefore we are probing possible modifications of the gluon structure function in a nucleon in the presence of nuclear matter.

1.2.1 Differential Cross Section

At large momentum transfer (greater that 1 GeV), or equivalently at short distances, the coupling constant of the strong interaction tends to zero, and therefore partons are essentially free particles. This QCD property is known as asymptotic freedom. The quantum mechanical amplitude of a process is calculated by adding the amplitudes of all the Feynman diagrams that contribute to that process.[8] Since at high momentum transfer the coupling constant becomes very small, the amplitude of a process can be calculated by adding the contributions of the lowest-order subprocesses.[9] Higher-order subprocesses only add corrections to the lowest-order subprocesses.

The lowest-order QCD subprocesses for J/ψ production in proton-nucleon collisions are quark-antiquark annihilation and gluon-gluon fusion (Fig. 1.2). To obtain the differential cross-section in hadron-nucleon collisions we need to multiply the cross section for each subprocess by the structure functions (distribution functions) of the partons involved in each interaction.

For beam energies greater than 100 GeV, J/ψ production is dominated by

[8]Each vertex in a Feynman diagram introduces a coupling constant to the amplitude of that subprocess.

[9]The Feynman diagrams with the smaller number of vertices.

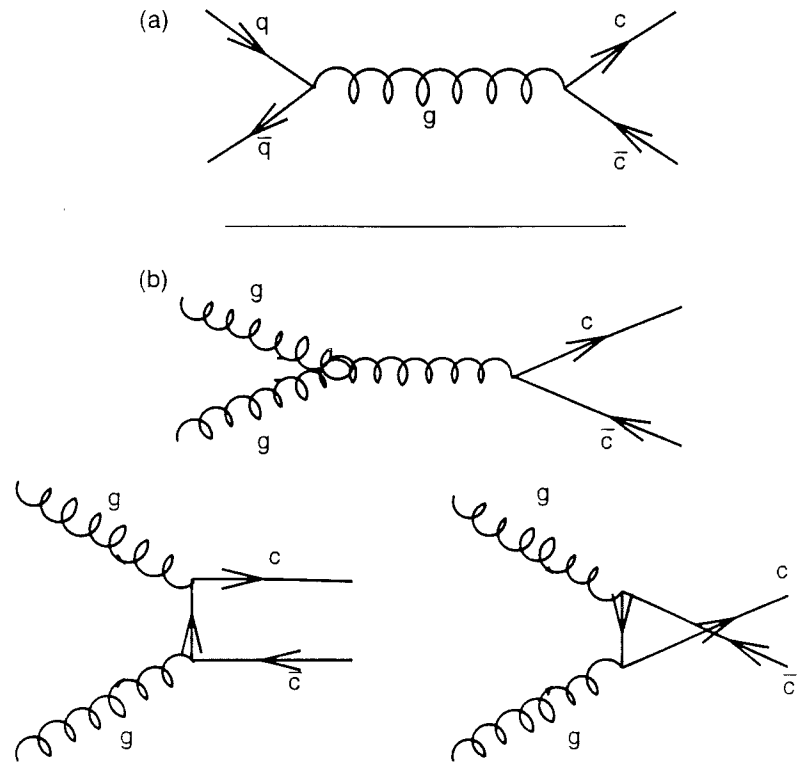

Figure 1.2: Lowest-order QCD subprocesses for J/ψ production. (a) quark-antiquark annihilation and (b) gluon-gluon fusion (three diagrams in the gluon-gluon fusion process are necessary to assure Gauge-invariance).

gluon-gluon fusion; quark-antiquark annihilation contributes only 10% to the total cross section [12]. In this experiment, since the beam energy is 800 GeV, gluon-gluon fusion is the dominant subprocess.

1.3 Nuclear Dependence of the Cross Section

The dependence of the cross section on the atomic weight, A, is known as nuclear dependence or A-dependence. In order to compare cross sections of heavy and light nuclei, the nuclear dependence of cross sections is commonly parametrized by the equation

$$\sigma_A = A^\alpha \sigma_N, \tag{1.1}$$

where σ_N and σ_A are the cross sections of a free nucleon and a nucleus, respectively, and A is the atomic weight of the nucleus. The differential form of this equation is

$$\frac{d\sigma_A}{dx} = A^\alpha \frac{d\sigma_N}{dx}, \tag{1.2}$$

where dx is the differential of some kinematical variable, for example x_F, p_t, x_1. α is experimentally measured by comparing production cross sections on heavy targets with those on light targets. The J/ψ-nuclear-dependence experimental results show that cross sections per nucleon for heavy nuclei are lower than for light nuclei, implying that scattering in bound nucleons is different than in free nucleons [14]. This result might be due to the same phenomena responsible for the EMC effect (which is not yet well understood). Also, it might be related to some QCD effects. Since there is not a complete explanation of the nuclear dependence of J/ψ production, in this experiment we are increasing the x_F

range of measurements to the region near zero to provide more data for the study of these phenomena. E789 also performed a J/ψ nuclear dependence experiment at large x_F covering the kinematic range $0.3 < x_F < 0.95$ on beryllium and copper targets extending the range of measurements at high x_F. In that experiment, a nuclear suppression of J/ψ production on heavy nuclei at high x_F was confirmed [13]. The results are consistent with previous results obtained in E772 [14].

Chapter 2
APPARATUS

2.1 Apparatus Overview

The E789 spectrometer (Fig. 2.1), designed to measure two-body decays of neutral c- and b-quark hadrons, is a slightly modified version of the E605/E772 apparatus [15]. The modifications consisted of replacing the multiwire proportional chambers by drift chambers and adding silicon detectors just downstream of the target [1]. The spectrometer detected single particles at high transverse momentum and oppositely-charged pairs at high invariant mass. For the J/ψ nuclear dependence experiment the main parts were: a rotating-wheel target holder, two big magnets, and a tracking detector. The rotating-wheel target holder held the three targets used in the experiment. The magnets swept away low-momentum particles and focused high-transverse-momentum particles onto the downstream detectors. The momentum of a charged particle was determined by the measurement of the deflection of its track when traversing the known magnetic field.

In this analysis we will define a right-handed coordinate system, with the z-axis pointing along the beam, the y-axis pointing up, and the x-axis pointing in the horizontal direction. The origin of the coordinate system is at the upstream end of the SM12 magnet.

Figure 2.1: The E789 spectrometer.

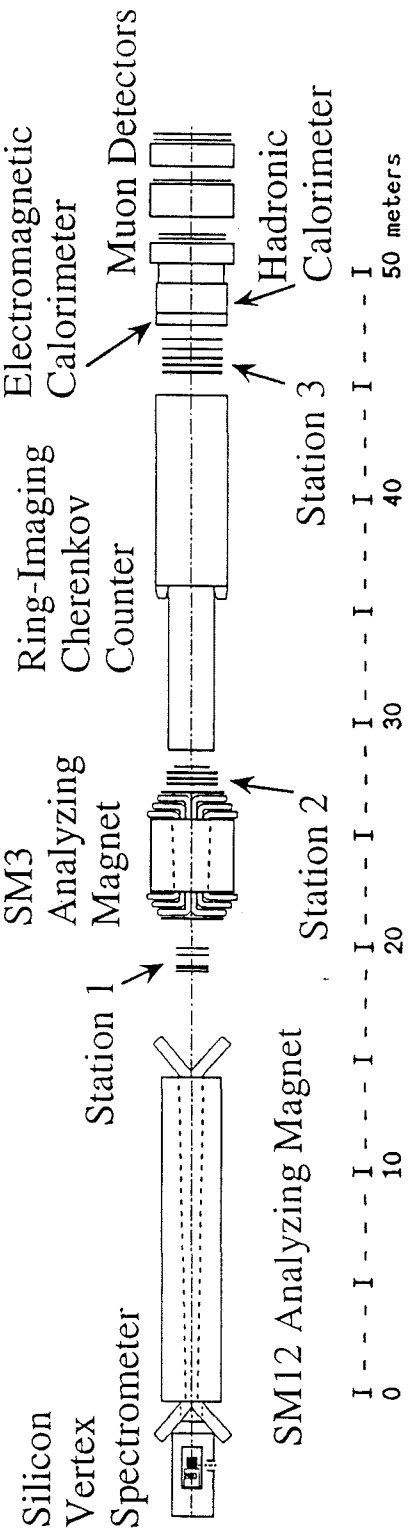

2.2 Beam

Protons were accelerated in the Fermilab Tevatron to an energy of 800 GeV and sent every 19 nanoseconds to the Meson-East beam line in bursts called "RF buckets." The duration of each bucket was $\approx$ 1 nanosecond. Buckets were grouped into spills. A spill lasted typically 22 seconds and thus contained 10^9 buckets. The time between spills was approximately 40 seconds. The intensity of the beam for this run was up to $\approx 10^{11}$ protons per spill.

2.3 Targets and Targeting Monitors

There was a wire target of platinum (Pt) located at $z = -130''$ and a rotating target wheel, with beryllium (Be), carbon (C), and tungsten (W) targets, at $z = -80''$ (target characteristics are listed in Table 2.1) [16].[1]

Table 2.1: Target characteristics

Target	Atomic Number (Z)	Atomic Weight (A)	thickness (inch)	Diameter (inch)	Density (g/cm^3)
Be	4	9.01	0.958	2	1.848
C	6	12.01	0.800	2	2.21
W	74	183.85	0.1175	2	19.3

Before every spill, the target wheel was rotated, bringing a different target into position. This procedure allowed us to reduce systematic uncertainties due to efficiency changes in the detector and long term drifts in beam tuning,

[1]The targets in this experiment were also used in E772. Target characteristics were taken from E772 logbook, volume 0, pages 168-171.

making easier and more reliable the target-to-target normalization for the nuclear-dependence ratios.

Two shielded scintillation telescopes viewing the platinum target at an angle of 90° detected particles produced in the platinum target. An ion chamber and a secondary emission monitor in the beam line detected the protons in the beam. The number of counts from the ion chamber and the scintillation telescopes gave us a way of looking at the focus and the intensity of the beam. In every spill the total counts of the ion chamber and the 90° scintillation telescopes were recorded on tape for off-line analysis.

2.4 Magnets

Two opposite-polarity dipole electromagnets, called SM12 and SM3, were used to focus the particles into the detectors and measure their momenta. SM12 also swept away low-momentum charged particles. The SM12 magnet, extending from $z = 0''$ to $z = 572''$, was operated at a current of 1411 amperes, while SM3, extending from $z = 848''$ to $z = 974''$, was operated at a current of 4214 amperes. These currents were set to maximize the acceptance for J/ψ decays with x_F between -0.1 and $+0.1$.

2.5 Beam Dump

To intercept the non-interacting beam as well as low-transverse-momentum and neutral secondary particles, a beam dump of water-cooled copper was located inside SM12. The distance between the beam dump and the target was sufficiently large to allow events produced in the target to be distinguished

from those produced in the beam dump (Fig. 2.2.)

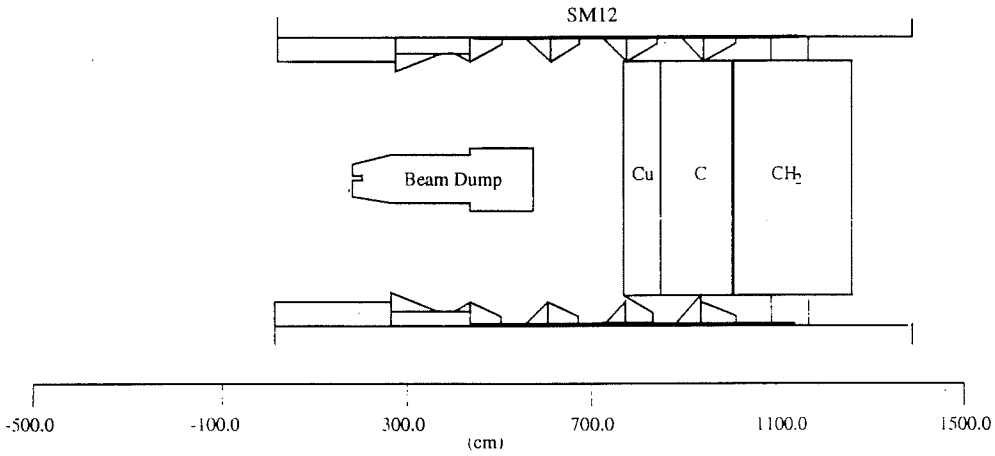

Figure 2.2: Elevation view of the SM12 magnet and the beam dump.

2.6 Detectors

The tracking part of E789 consisted of 18 drift-chamber planes, 7 hodoscope planes, 3 proportional-tube planes, 8 silicon-microstrip-detector planes, a calorimeter, and a ring-imaging Cherenkov counter. The silicon detectors, the calorimeter, and the ring-imaging Cherenkov counter were not used in this analysis.

Several tracking detectors and one or two scintillation hodoscopes were grouped to form a station. There were five stations numbered from 0 to 4. All the detectors except those of station 0 were located downstream of SM12. Station 1 was located between the SM12 and SM3 magnets. After the SM3 magnet there were station 2, the Cherenkov counter, station 3, and the

calorimeter. Behind the calorimeter there was an absorber wall and at the end there was station 4, where we detected only the muons produced in the interactions.

2.6.1 Scintillation Hodoscopes

Because scintillation counters have faster time response than drift chambers, scintillation hodoscopes were used to select muon tracks in the fast trigger and to eliminate out-of-time chamber hits in off-line analysis. The hodoscopes were made of strips of NE110 plastic scintillator each attached at one end by a Plexiglas light guide to a Hamamatsu R329 photomultiplier tube. The hodoscope planes were called X or Y depending on the orientation of the strips. The planes were also divided in half: x-hodoscopes had up and down halves (XU, XD) while y-hodoscopes had left and right ones (YL, YR.)

Dimensions and positions of the hodoscopes are given in Table 2.2.

Table 2.2: Hodoscope characteristics

Detector Name	Z-Position (in)	Aperture x(in) $\times$ y(in)	Channels $x \times y$	Cell Width (in)
$Y1$	770.00	47.38 $\times$ 30.688	2 $\times$ 12	2.557
$X1$	771.50	47.54 $\times$ 30	12 $\times$ 2	3.962
$Y2$	1114.94	64.5 $\times$ 48.625	2 $\times$ 16	3.039
$X3$	1822.00	105.18 $\times$ 92	12 $\times$ 2	8.765
$Y3$	1832.00	104 $\times$ 92	2 $\times$ 13	7.077
$Y4$	2035.50	116 $\times$ 100	2 $\times$ 14	7.143
$X4$	2131.12	126 $\times$ 114	16 $\times$ 2	7.875

2.6.2 Wire Chambers

Two types of chambers were used: drift chambers (DC) for stations 1 through 3, and proportional-tube counters (PT) for station 4. Stations 1 through 3 each had a set of six drift-chamber planes.[2] At each of these three stations, there were two drift-chamber planes for each of the axes y, u, and v. The u and v axes were oriented at angles $\theta = \pm \arctan(1/4)$ with respect to the y axis. Three orientations of drift chambers are necessary to remove position ambiguities when more than one hit are registered. The orientations of u and v were chosen to increase resolution in the y (magnetic deflection) direction, providing a greater accuracy of momentum measurement. In each station, the two planes for each axis were offset by half of a cell with respect to each other. Station 4 consisted of a set of three proportional-tube planes measuring x and y coordinates. Only muons were detected at station 4 because electrons and hadrons were stopped in the calorimeter and absorber wall.

The gas mixture for the drift chamber and proportional tubes was 50% argon and 50% ethane bubbling through ethyl alcohol at $-6°$C.

Table 2.3 summarizes the wire chamber characteristics.

[2]In E605/E772, station 1 had six multiwire proportional chambers.

Table 2.3: Wire chamber characteristics

Detector Name	Type	Z-Position (in)	Aperture x(in)$\times y$(in)	Channels
V1	DC	740.08	47×32	208
V1′	DC	742.13	47×32	208
Y1	DC	749.80	47×32	160
Y1′	DC	751.85	47×32	160
U1	DC	759.96	47×32	208
U1′	DC	762.01	47×32	208
U2	DC	1083.40	66×51.20	160
U2′	DC	1085.52	66×51.20	160
Y2	DC	1093.21	66×51.20	128
Y2′	DC	1095.33	66×51.20	128
V2	DC	1103.25	66×51.20	160
V2′	DC	1105.37	66×51.20	160
U3	DC	1790.09	106×95.5	144
U3′	DC	1792.84	106×95.5	144
Y3	DC	1800.20	106×91.84	112
Y3′	DC	1802.95	106×91.84	112
V3	DC	1810.24	106×95.50	144
V3′	DC	1812.99	106×95.50	144
PTY1	PT	2041.75	117×120	120
PTX	PT	2135.875	135×121.5	135
PTY2	PT	2200.75	141.3×143.1	143

Chapter 3
DATA ACQUISITION AND REDUCTION

The data acquisition system was the same as in E605/E772 (Fig. 3.1). It consisted of a triggering system, a readout system, a large high-speed buffer memory,[1] and an on-line computer.

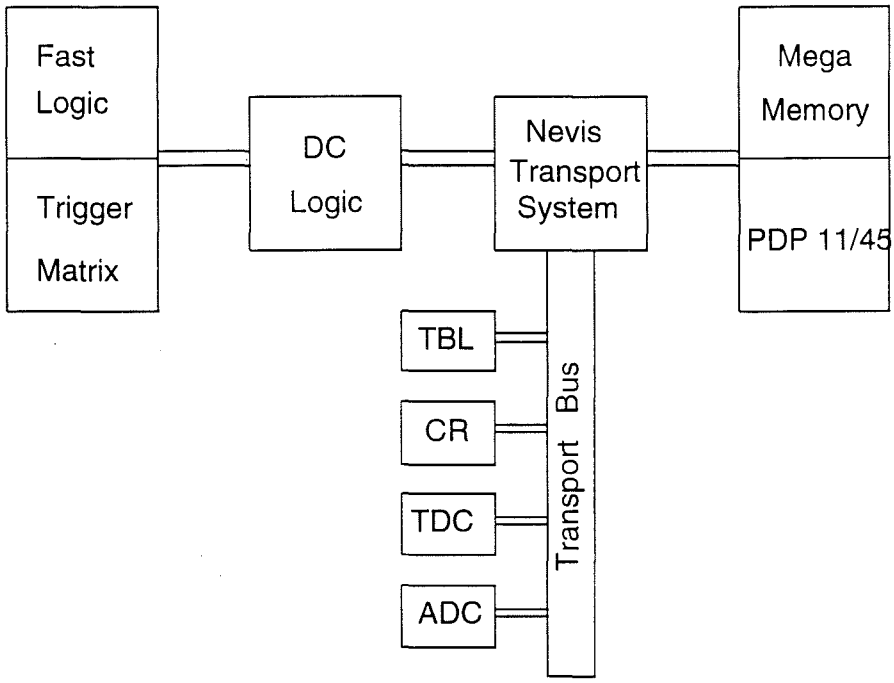

Figure 3.1: Block diagram of the data-acquisition system.

[1] Called the Megamemory

3.1 Triggering System

The aim of the triggering system was to distinguish the interesting events (in our case dimuon events produced in the target) from the background reducing as much as possible the number of uninteresting events recorded on tape and reducing consequently the amount of off-line analysis. The triggering system had three levels. The first-level trigger (fast trigger) selected dimuon events and rejected pairs consisting of two muons from different RF buckets (i.e. from the same spill but different bursts). It reduced the trigger rate sufficiently so that the second-level (DC logic) and the third-level (trigger processor) triggers could make further decisions with small dead time. The third-level trigger was not used in this experiment.

3.1.1 First-level Trigger

Signals from the hodoscopes were the input to the fast-logic trigger. To reject pairs of muons associated with different RF buckets, and therefore achieve single-RF-bucket timing resolution, the hodoscope signals were first synchronized to the accelerator RF signal by "pulse stretcher" modules [17]. The signals were then fanned out to coincidence register (CR) cards, trigger matrix modules, multiplicity logic units, and hodoscope terminator modules.

The hodoscope terminator modules formed the logical OR of each half-bank of counters; their outputs went to coincidence circuits set to require three hits out of four in the hodoscope planes $X1$, $Y1$, $X4$, $Y4$. These coincidences, called $\frac{3}{4}\mu L$ and $\frac{3}{4}\mu R$, defined tracks traversing the entire apparatus, and mostly corresponded to high-momentum muons. A dimuon trigger was formed by

requiring $\frac{3}{4}\mu L \odot \frac{3}{4}\mu R$ (designated $\frac{3}{4}\mu LR$ in the scalers).[2] Prescaled single-muon triggers[3] ($\frac{3}{4}\mu L$, $\frac{3}{4}\mu R$) and the dimuon trigger ($\frac{3}{4}\mu LR$) were OR'ed together by the Trigger-Fan-In module to form the TFI signal which started the second-level trigger.

3.1.2 Second-Level Trigger

The Trigger-Fan-In signal (TFI) from the Fast Logic came to the Trigger-Generator-Input (TGI) module which strobed the logic-bus CRs and triggered the DC-logic decision cycle. If any of the DC-logic modules' criteria was satisfied, the DC logic sent a signal to the Trigger-Generator-Output (TGO) module that started the readout system. If, on the other hand, the DC-logic criteria were not satisfied, then the readout system was reset, and at the end of the DC-logic deadtime another TFI could be accepted.

The TGI produced a busy signal during the DC-logic cycle to block incoming triggers. Similarly, the TGO accepted a hold signal from the readout system during the readout cycle. These two signals were fanned in to form the system busy (SB) signal, which was used to monitor system live-time.

The DC logic, which is described in detail in reference [18], was a flexible general-purpose triggering system that could generate up to 16 different logical trigger coincidences. It consisted of a set of "pin-logic" modules that performed logical operations: each module formed the "and" of any of 16 logic-

[2] $\odot$ and $\oplus$ refer to the logical operators AND and OR respectively.

[3] The single-muon triggers were prescaled by 4K (4096). Single muons are prominently produced in hadron decays, therefore it was necessary to prescale the single-muon triggers in order to prevent the megamemory from being filled with such data.

bus signals or their complements. Input signals to the logic bus were strobed by the TFI signal and latched by CRs so that further processing could be done with DC levels without worrying about timing. The outputs of each pin-logic module included a trigger signal and complementary logic signals that could be connected to other pin-logic module inputs. The front panel also had also an "inhibit" input for prescaling, and scaler outputs with or without dead time.

3.2 Readout System and Megamemory

The readout system consisted of a Nevis transport system [19], and the data conversion subsystems ADCs (Analog to Digital Converters), TDCs (Time to Digital Converters), and CRs (Coincidence Registers).[4] The Nevis transport system served as the interface between the data conversion systems and the buffer memory. Its purpose was to receive parallel data streams from external sources and organize them into an output data stream. The transport system was controlled by the presence of data itself, rather than by a central controller. Transport read out all information from each data conversion subsystem and stored on it in the megamemory [20]. The megamemory was a fast buffer that could store four megabytes of data per spill; up to 4092 events per spill could be stored.

At the end of each spill, the PDP-11 on-line computer dumped the part of

[4]The ADCs were used to read out pulse heights from the calorimeter and the Cherenkov counter, the TDCs were used to read out the drift times of the drift chambers, and the CRs were used to read out the hodoscopes, the proportional tubes, and the silicon strip detectors.

the megamemory contents containing the new data onto 6250-BPI magnetic tape.

3.3 Data Reduction

In the J/ψ nuclear-dependence experiment approximately 120 6250-BPI tapes were recorded from May to July, 1990. The analysis of these tapes was divided into three stages: the first pass found muon tracks using information from the hodoscopes and drift chambers; to eliminate any non-muon tracks it also required hits along the track in station 4.

The second pass traced the tracks back towards the target in steps using the SM12 field map. It made aperture cuts at various points in the SM12 magnet and required that each event have two tracks that pointed to the target.

The third pass used the track directions and momenta to calculate physics quantities.

The quality of the data was examined spill by spill using the scaler monitors. Scaler cuts were made to get rid of spills that were taken when the detector had poor performance due to beam problems or to malfunctions of some elements of the detector. These cuts were introduced in the third pass to discard potentially bad events.

Chapter 4
SCALER ANALYSIS

A scaler is an electronic device that counts detector pulses from discriminators[1] and fast logic modules. It transforms the counts received over a given period of time into parallel binary data words which can then be presented to a centralized display and a computer by commands from a control system. Basically, it has a START, a STOP, and a RESET signal. The START signal initiates the accumulation of data. The STOP signal finishes the process. The RESET signal clears the memory and readies the scaler to make another measurement (some scalers have also a clock mechanism that allows preselecting a desired counting time). A NIM scaler should be able to accept NIM pulses[2] at a high speed and also be able to generate only one pulse when wide input signals are received. Common scalers used in experimental high energy physics provide 24 bits of data storage capacity ($\approx$ 17 million counts) and can count pulses at a 100 MHz rate.

The purposes of the scalers in the experiment were twofold: monitoring the apparatus performance and providing data needed for normalization of cross

[1] A discriminator is an electronic device that accepts analog pulses from a detector. For each pulse that is above a threshold it delivers an output logic pulse.

[2] NIM stands for Nuclear Instrumentation Module. NIM modules are electronic devices such as discriminators and logic units with some standard requirements on voltage levels, rear connectors, dimensions, etc.

sections. Eighty-eight scalers were used in E789.[3] They measured variables such as beam intensity, magnet currents, target position, counts in hodoscopes, ion chamber, scintillation telescopes, etc.; and rates of trigger signals such as TFI, TGO, $3/4\mu$L, etc. After each spill, a computer program displayed the scaler counts on a CRT screen, and a separate program wrote them on tape preceding the event data from that spill.

This chapter introduces the expression for the differential cross section to see its dependence on apparatus and beam monitors. It also explains the off-line analysis performed on beam and apparatus monitors after the second pass. This analysis was necessary to select the appropriate cuts to use in discarding bad events, and to compare the redundant scalers and select the more reliable ones for the third-pass analysis.

The off-line scaler analysis was performed using the Physics Analysis Workstation (PAW) program [21]. This program enabled us to create scatter plots, histograms, and fits to histograms of the scaler variables in a very simple way. It also enabled us to examine spill by spill the various scaler variables described in this thesis. In order to analyze the data using PAW a two-dimensional array file, called an n-tuple, was created. The scaler values from each spill were grouped by run numbers in the n-tuple file. To distinguish spills from different runs I have introduced a new variable called *ABSPILL*. *ABSPILL* was generated by reading spills from the n-tuple file and assigning sequentially-increasing numbers to each spill. The run a spill belonged to was not taken into account in the process of assigning numbers to spills. Throughout this

[3] A list of the scalers used in the experiment is included in appendix A:.

work I will refer to what I have named absolute spill number, *ABSPILL*, as spill. When I want to refer to spills belonging to a specific run I so indicate.

4.1 Differential Cross Section

The differential cross section in a bin x of width dx is given by

$$\frac{d\sigma}{dx} = \frac{N_{ev}}{N_{inc}} \frac{A}{N_A \rho t \varepsilon \eta l} \frac{1}{dx}, \tag{4.1}$$

where

x = some kinematic variable of interest (e.g. x_F, p_t),

N_{ev} = number of events in the bin x,

N_{inc} = number of incident protons,

A = atomic weight of the target material,

N_A = Avogadro's number,

ρ = density of the target,

t = target thickness,

l = live time,

ε = efficiency,

η = acceptance.

Live time is a correction made for interactions that occurred during trigger or readout electronics dead time. The acceptance is defined as the fraction of muon pairs emerging from the target which traverse the spectrometer and satisfy the trigger-hodoscope geometrical requirements. The efficiency is the

fraction of pairs satisfying the acceptance which satisfy the trigger logic and pass the various track reconstruction and analysis cuts.

In this experiment we were interested in the ratio of the cross-sections for different targets rather than the absolute cross-section for each target. Using Eq. 4.1, the ratio of the cross-sections for two targets, i and j, is

$$R_{ij} = \frac{\sigma_{A_i}}{\sigma_{A_j}} = \frac{(N_{ev})_i}{(N_{ev})_j} \frac{(N_{inc})_j}{(N_{inc})_i} \frac{A_i}{A_j} \frac{\rho_j}{\rho_i} \frac{t_j}{t_i} \frac{\varepsilon_j}{\varepsilon_i} \frac{l_j}{l_i}. \tag{4.2}$$

Acceptances cancel since the same apparatus was used for all the targets and targets were interchanged every spill. From this equation we see that besides the number of events produced in each target and the flux incident on each target, we also need to know target densities and thicknesses (Table 2.1) and efficiencies and live time for each target. The parameter α used to study the nuclear dependence (Eq. 1.1) is then given by

$$\alpha = \frac{\ln\left(\sigma_{A_i}/\sigma_{A_j}\right)}{\ln\left(A_i/A_j\right)} = \frac{\ln R_{ij}}{\ln\left(A_i/A_j\right)}. \tag{4.3}$$

To calculate R_{ij} it is necessary to separate spills by target, calculate live time and beam fluxes for each target, and study the apparatus and beam performance for each spill.

4.2 Apparatus Monitors

The apparatus monitors here described are the ones required for target identification and for monitoring live time and magnet currents for each spill.

4.2.1 Target Selection

To compute α, it is essential to know which target was in the beam in each spill. Two scaler monitors, *TARGET* and *ME6COM*, were used to specify which target was in the beam. To find out how the target monitors were working during the experiment I plotted them versus spill number (Fig. 4.1). For both target scalers the plots show four horizontal lines corresponding to the four positions of the target wheel. From the figure, we observed that the *TARGET* scaler was not working during some spills. That is, in some spills the *TARGET* scaler registered values close to zero while the corresponding spills on *ME6COM* displayed values different than zero (spills numbers 179-1335). In addition, we noticed that both scalers presented some spills with values on none of the four lines corresponding to the four positions of the target wheel. The *TARGET* scaler presents more spills scattered out of these lines than *ME6COM*. We found out as well that there were spills in which *TARGET* and *ME6COM* scalers disagreed in recording which target was in the beam.

For those spills where *TARGET* and *ME6COM* disagreed in which target was in the beam, I looked for scalers with target dependence. Figs. 4.2 and 4.3 present the behavior of the *Y1R3/SEM3*, *Y1R3/SEM4*, *X3L7/SEM3* , and *X3L7/SEM4* versus spill.[4] Although all these plots exhibit a target dependence, the four lines corresponding to the different targets are better distinguished in the scatter plot of *Y1R3/SEM3* versus spill. For most of the spills where the target scalers disagreed, by looking at the ratio *Y1R3/SEM3*

[4]The reason for the jumps observed on the vertical axis when the scaler *SEM3* is used to form a ratio in Fig. 4.2 will be discussed in the study of the beam-intensity monitors.

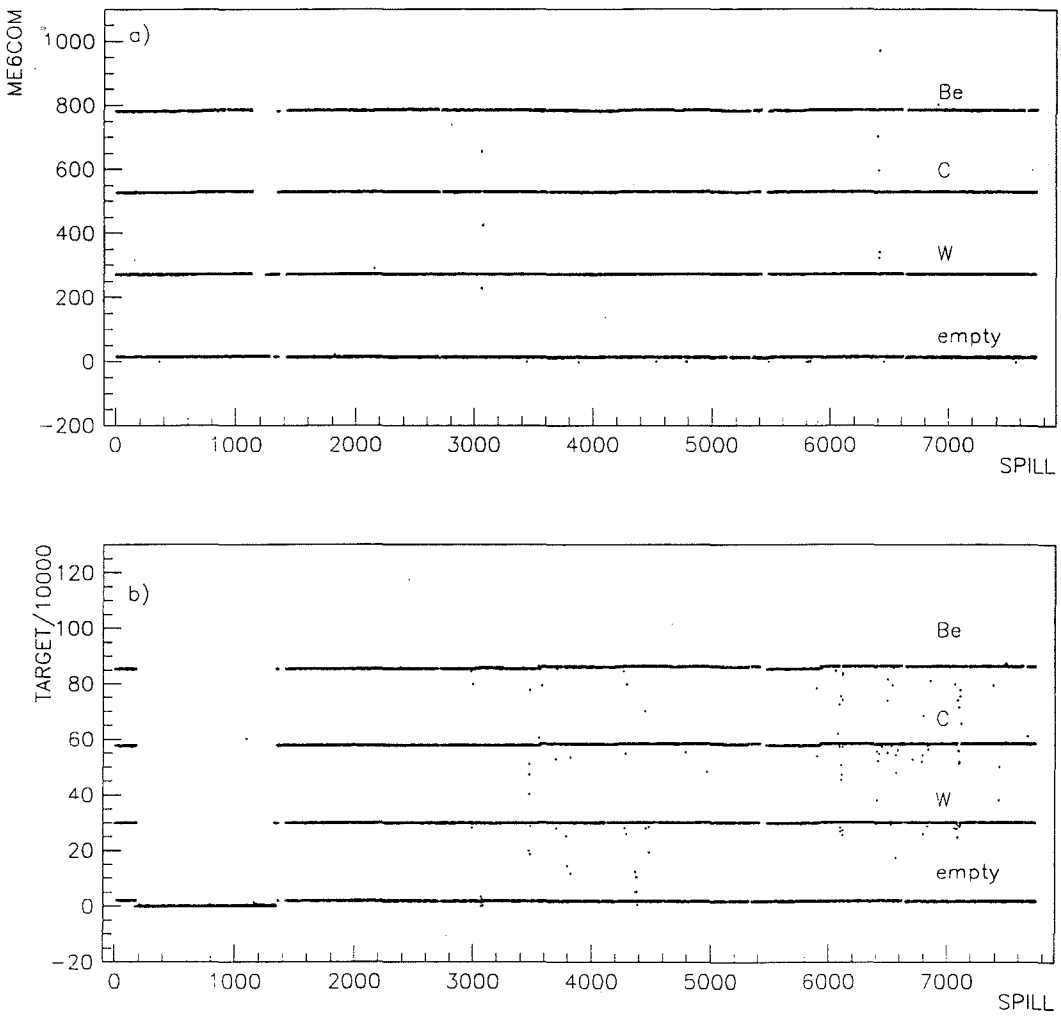

Figure 4.1: Target selection scalers versus spill. The four horizontal lines correspond to the four positions of the target wheel. The scaler *ME6COM* was more reliable than the *TARGET* scaler.

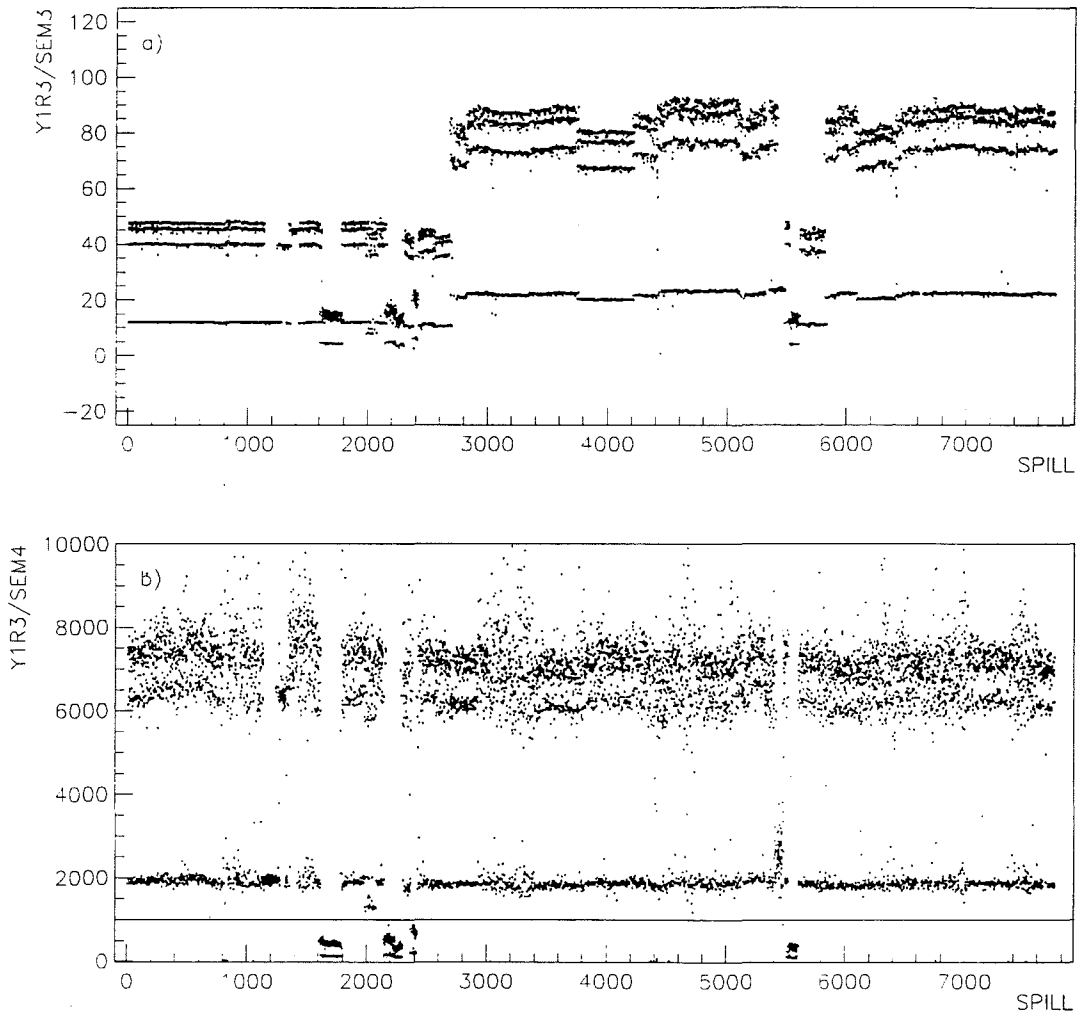

Figure 4.2: Ratios formed by the *Y1R3* hodoscope counter and the beam intensity monitors. Spills below the horizontal line correspond to spills where the beam was far away from the center of the target (see discussion in section 4.3.1.b).

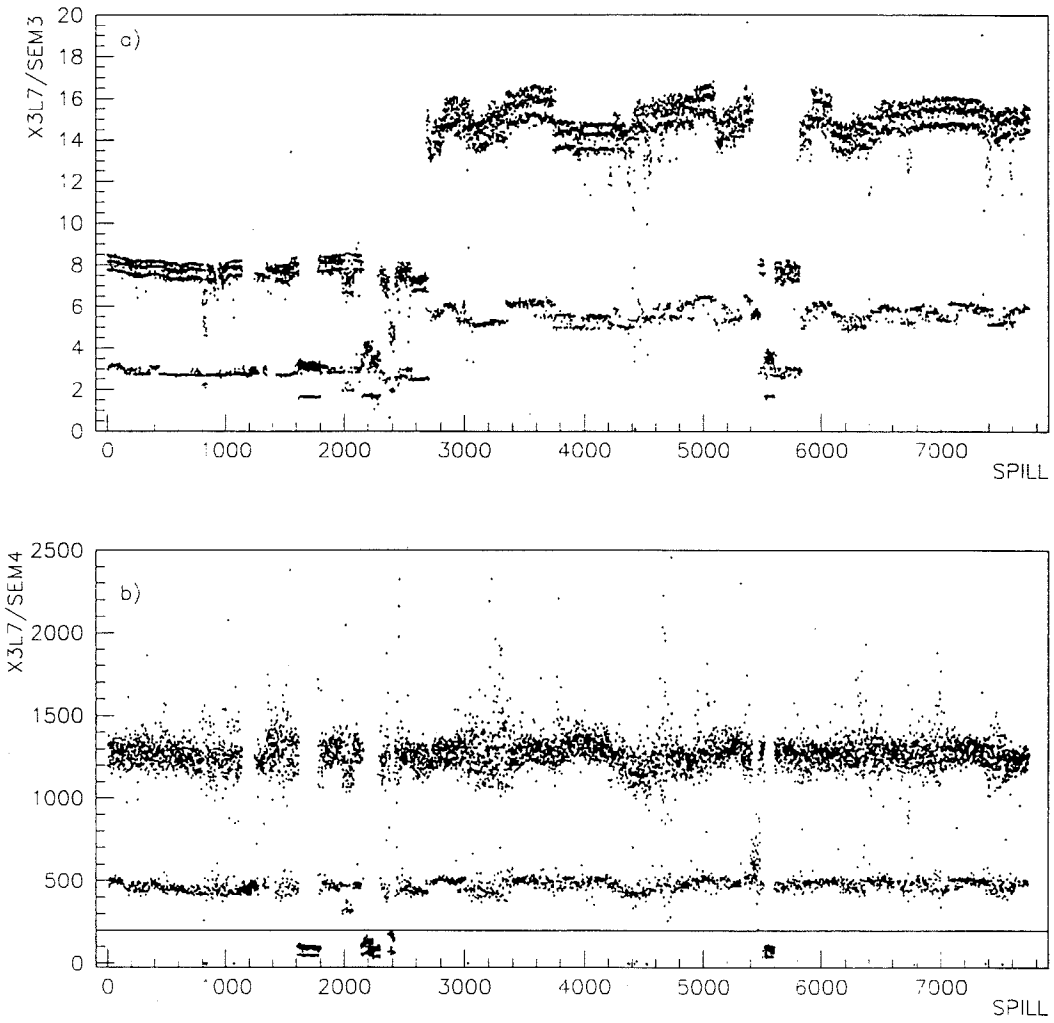

Figure 4.3: Ratios formed by the *X3L7* hodoscope counter with the beam intensity monitors. Comparing Fig. 4.2 and 4.3, *Y1R3* presents a stronger target dependence than *X3L7*. The target dependence is better observed when *SEM3* is used to form the ratio. Spills below the horizontal line correspond to spills where the beam was far away from the center of the target (see section 4.3.1.b).

for each spill, I was able to tell which target was in the beam. There were spills where I was not able to identify the target a spill belonged to because the value given by *Y1R3/SEM3* was not on any of the four lines. For those spills where the *TARGET* scaler was not working, *ME6COM* and *Y1R3/SEM3* disagreed in less than 1.5%. The disagreement is partly due to the fact that in some spills the values *Y1R3/SEM3* for the carbon and beryllium target were very close and they could not be separated (e.g. spills 2703-2852).

In the logbook[5] it was noted that at run 400 the target wheel was spinning continuously. Taking a closer look at the spills in run 400, using the *Y1R3/SEM3* ratio (Fig. 4.4), we found out that the target wheel was only spinning from spill 30 of run 400 to the end of the run, spill 33 (spills 6406 to 6409).

Since *ME6COM* was the most reliable target monitor we decided to use it in the third-pass analysis. We explicitly assigned targets to some spills where the *ME6COM* and *TARGET* monitors disagreed with each other, but we were able to conclude which target was in by inspecting the values of *Y1R3/SEM3*. *ME6COM* and *TARGET* scalers disagreed in less than 1%. A list of the spills with the assigned targets using the *Y1R3/SEM3* ratio and the discarded spills is included in Appendix C:.

In Fig. 4.1, starting from the lowest horizontal line and finishing with the upper line, the identity of the targets in both plots is: first the empty target; above it the tungsten, carbon, and beryllium targets are located. The same distribution of targets is found in *Y1R3/SEM3* and *X3L7/SEM3* plots in

[5]The logbook is a notebook where every incident related to the experiment is recorded.

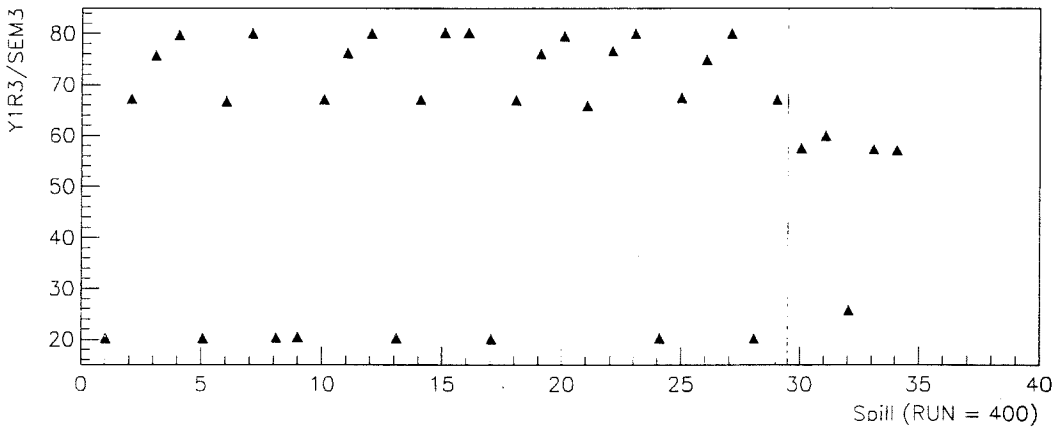

Figure 4.4: *Y1R3/SEM3* versus spill number for spills in run 400. The values of *Y1R3/SEM3* are unaligned after spill 29, when the target wheel started to spin (spills after the vertical line).

Figs. 4.2a and 4.3a respectively.

4.2.2 Live Time

There were moments during the data taking process in which either the readout system or the DC logic was not able to process more events. During those periods of time, known as dead time or recovery time, the sensitivity of the experiment was zero. In the off-line analysis we must correct for the event losses caused by dead time. Live time, in contrast to dead time, is the fraction of time in a spill in which the data taking system is ready to accept and process new events.

The scalers used to estimate live time in the experiment were *SEM3*, *AMON*, *WMON*, and *TFI*. To determine live time a system-busy signal was created. System busy was a logical OR of the DC-logic busy signal

and the readout-system busy signal. The complement of the system busy ($\overline{system\ busy}$) was put in coincidence with each of the scalers mentioned above, creating the signals *SEM3SB*, *AMONSB*, *WMONSB*, and *TFISB*. Live time is computed in the off-line analysis as

$$l = \frac{K_{\overline{SB}}}{K}, \tag{4.4}$$

where K is any of the signals used to measure live time, and $K_{\overline{SB}}$ is the coincidence of the signal with $\overline{system\ busy}$. Fig. 4.5 shows live time versus spill for all the live time scalers defined in the experiment. Notice that live time measured by the ion chamber, *SEM3*, is higher than live time measured by the other scalers because *SEM3* was a signal coming from an integrator. The gap observed in the *WMONSB/WMON* plot from 0.99 to 1.0 is due to the limit in the resolution of the *WMON* scaler. *TFISB/TFI* presents a handful of spills with very low values that are not seen in the rest of the scalers. The reason for those low values is that the dependence of *TFI* with the beam intensity was not always linear. The dependence of *TFI* with beam intensity is plotted in Fig. 4.6. Some groups of spills had atypically low live time, e.g. spill numbers 572-949, 4209-4269, 5409-5475, 5783-5821.

Table 4.1 contains the mean and RMS values of live time for each live time scaler. Mean values of live time measured by each scaler agree within 3%. The table shows that live time is target independent, therefore live time cancels out in the calculation the cross-section ratios (Eq. 4.2).

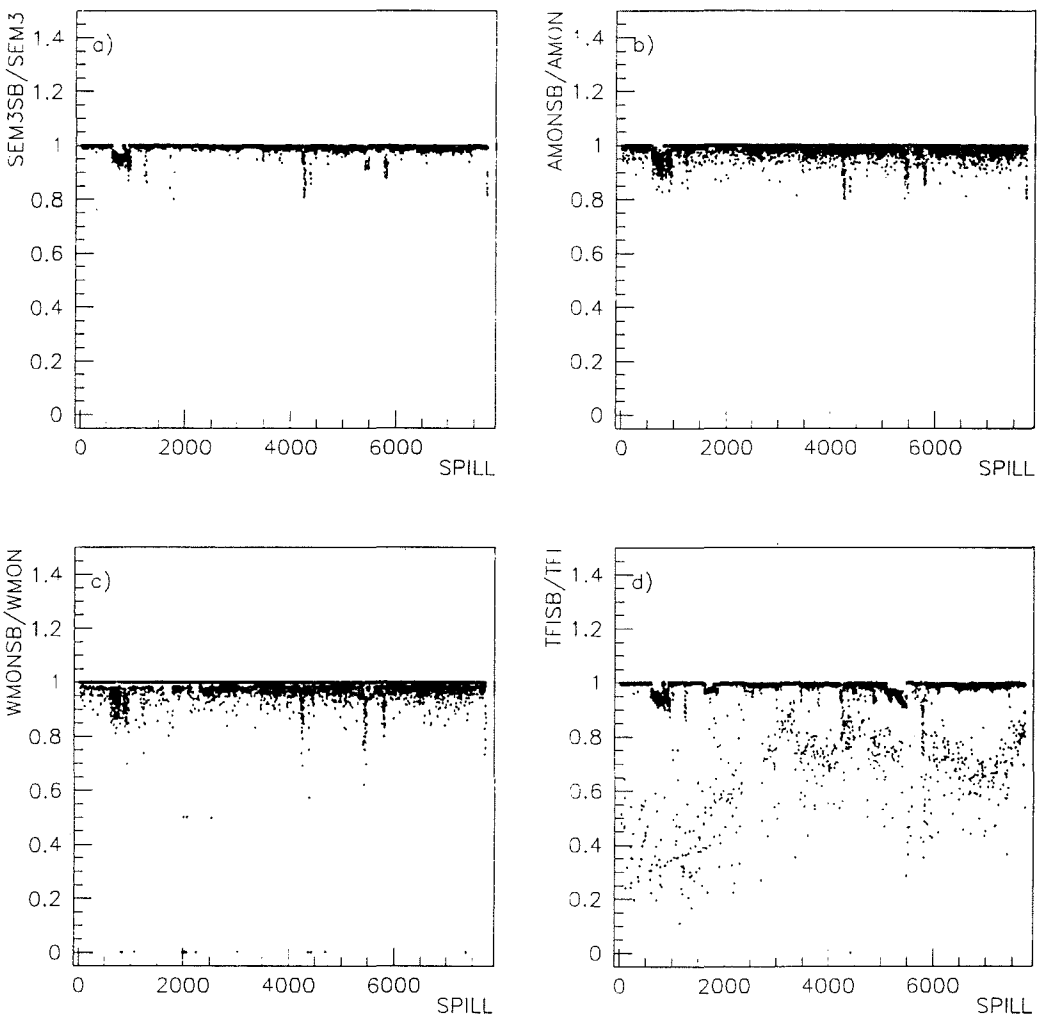

Figure 4.5: Live time versus spill. All live time monitors defined in the experiment have been included.

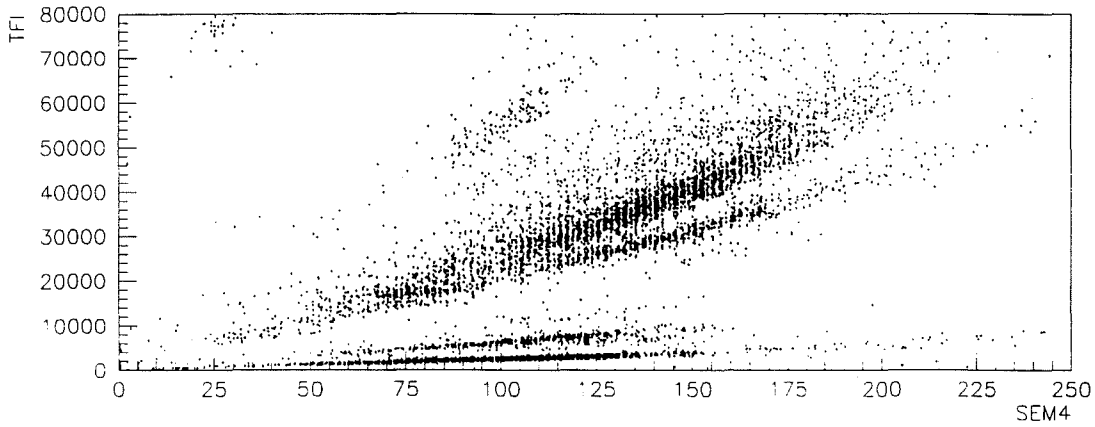

Figure 4.6: *TFI* versus *SEM4*. The dependence of *TFI* with the intensity of the beam was not always linear. I have not displayed spills with TFI higher than 8×10^4.

Table 4.1: Live time mean values and RMS for each scaler and each target.

	Empty		W		C		Be	
	Mean	RMS	Mean	RMS	Mean	RMS	Mean	RMS
SE3SB/SEM3	0.99	0.02	0.99	0.02	0.99	0.02	0.99	0.02
AMONSB/AMON	0.99	0.02	0.98	0.02	0.98	0.02	0.98	0.02
WMONSB/WMON	0.98	0.07	0.98	0.06	0.98	0.06	0.98	0.08
TFISB/TFI	0.96	0.1	0.96	0.1	0.96	0.1	0.96	0.1

4.2.3 Magnet Currents

The magnet currents of SM12 and SM3 were monitored by the scalers *SM12AI* and *SM3AI*. Their values per spill are shown in Fig. 4.7. *SM12AI* had 16 spills where the value recorded was zero. *SM3AI* had 21 spills where the value recorded was smaller than 600. These spills have not been shown in the figure to make visible the variations of the current in the rest of the spills. We did not cut out these spills because they were not consecutive and therefore it was very unlikely for the magnet currents to have made such abrupt changes in such a brief period of time. Table 4.2 gives the mean and RMS values of both magnet currents. The magnet current varied less than 0.03% RMS and less than 0.05% RMS for the *SM12* and *SM3* magnets respectively.

Table 4.2: Mean and RMS values of the magnet currents.

	Mean	RMS
SM12AI	1141	0.35
SM3AI	4214	2.0

The magnet currents were very stable during the experiment.

4.3 Beam Monitors

Beam monitors were used to monitor the total beam intensity and its uniformity.

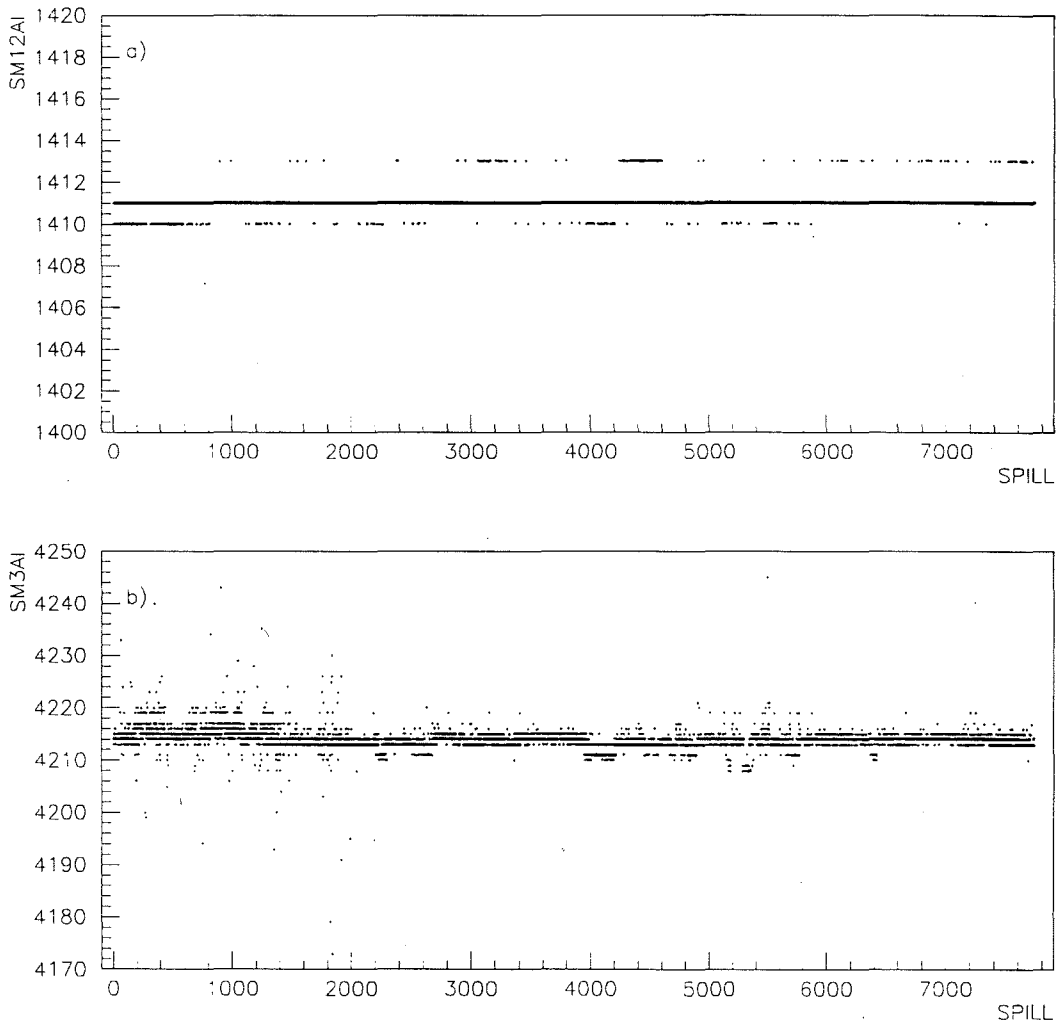

Figure 4.7: Magnet current scalers versus spill. The values of the magnet current are both very stable. *SM3AI* fluctuated slightly more than *SM12AI*.

4.3.1 Beam Intensity

Scalers *AMON*, *WMON*, *SEM4* and *SEM3* were used to monitor the incident beam flux. The scintillation telescopes *AMON* and *WMON* viewed the platinum wire target at 90°, so their counts were proportional to the number of interactions in the platinum wire. The ion chamber, *SEM3*, and the secondary-emission monitor, *SEM4*, provided signals proportional to the beam intensity. Since these four scalers give values proportional to the intensity of the beam we can calculate the total incident flux on each target by multiplying the readings of these scalers by their corresponding calibration constants. However, since in this experiment we are calculating the cross-section *ratios* between targets, we do not need the total beam flux hitting each target. We only need the beam fraction for each one.

The behavior of the beam-intensity monitors per spill is displayed in Figs. 4.8 and 4.9. These figures show that the counts of the beam-intensity monitors were changing almost every spill. Changes in the beam-intensity scalers could be due to changes in either the intensity of the beam or the calibration (or possibly saturation) of the monitors. In addition, in the case of the scintillation telescopes, changes could have been produced by variations in the aim or focus of the beam.[6]

[6] A defocussed or mis-steered beam will decrease the number of interactions in the platinum wire because only part of the beam hits the wire target. The other targets were wider (2 inch diameter) and all the beam was hitting them.

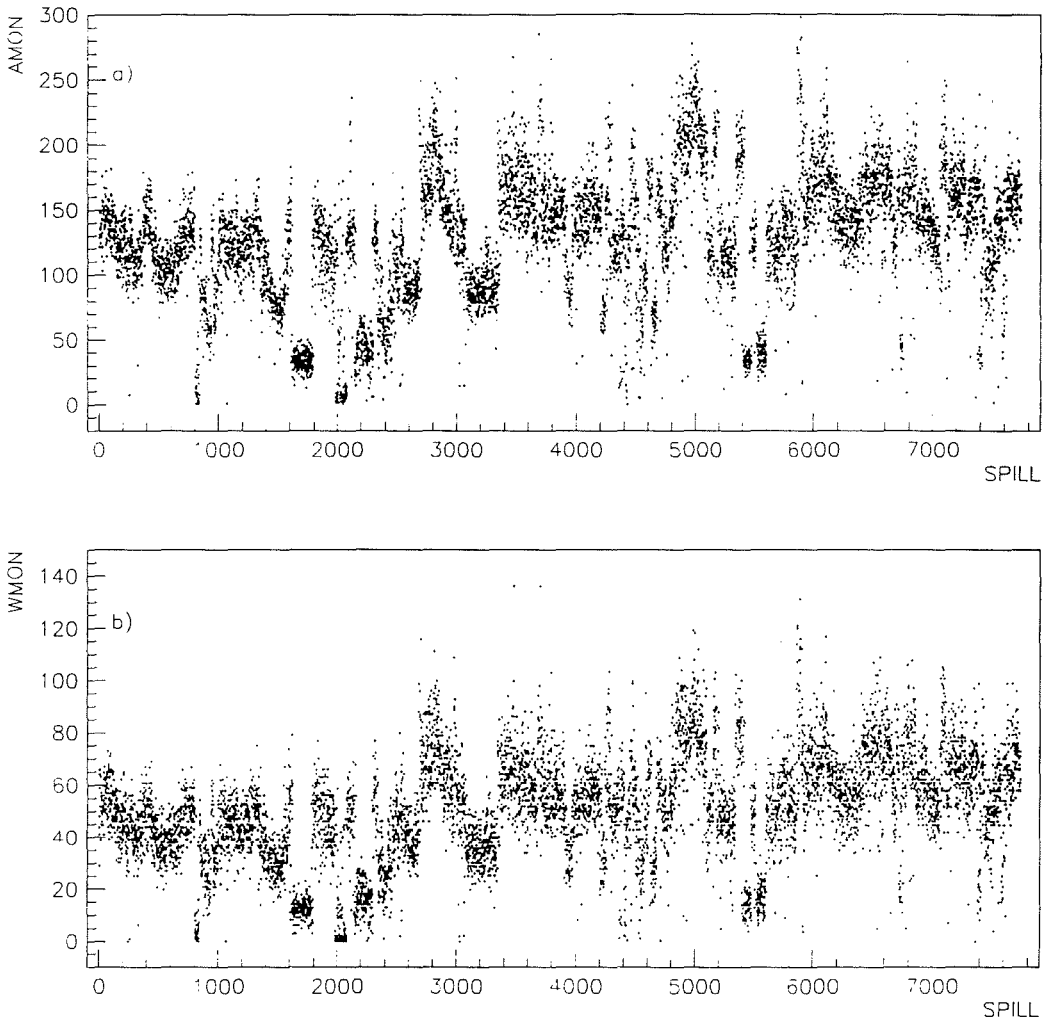

Figure 4.8: Values of the 90° scintillation telescopes versus spill. The observed changes of these monitors in almost every spill are due to changes in the experiment conditions beyond our control.

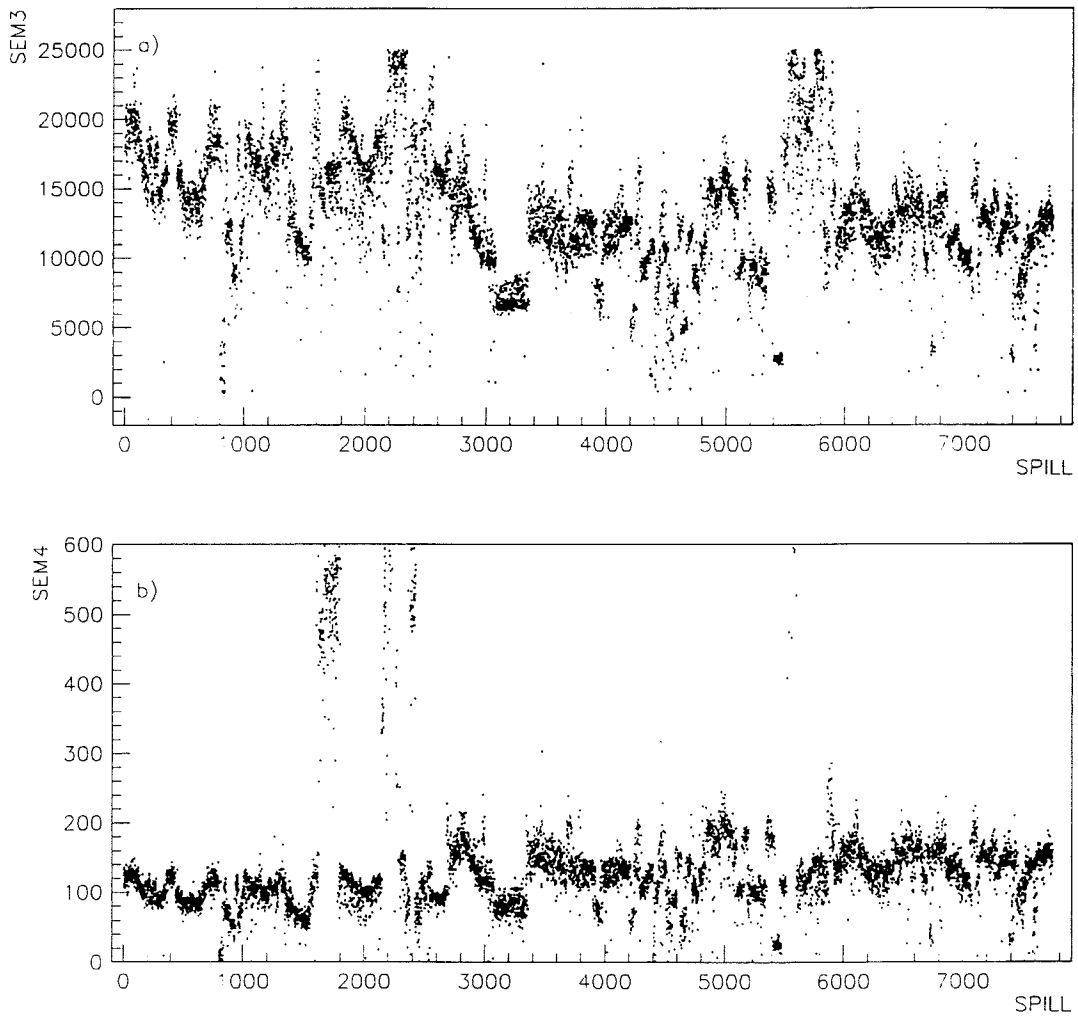

Figure 4.9: Values of *SEM3* and *SEM4* monitors versus spill. As in Fig. 4.8, the observed variations of these monitors in almost every spill are due to changes in the experiment conditions beyond our control.

4.3.1.a Changes of the Beam Intensity Monitors

To investigate the source of the changes in the beam scalers I plotted the ratios of the scalers *SEM3*, *SEM4*, *AMON*, and *WMON* versus spill number. Changes in the beam intensity should affect all of these scalers in the same way. Consequently for stable conditions and negligible offsets in the measurement devices, the values of these ratios would be constant. Fig. 4.10 shows ratios to *SEM3* and Fig. 4.11 shows other beam-intensity ratios. In Fig. 4.10 we observe that the *SEM3* ratios exhibit some changes during the experiment. The changes occurred at the same spill numbers for the three ratios plotted and are observed after spill number 2687,[7] where apparently the values of *SEM3* suffered a reduction of almost half. Less abrupt changes are also observed, for example at spill numbers 3746-4375. The remaining beam-intensity ratios, however, are almost constant during the experiment (Fig. 4.11). The changes in *SEM3* are also displayed in Fig. 4.12 where I have plotted *SEM4* versus *SEM3*. The data in the figure are mainly distributed along two lines of different slope, which shows that *SEM4* and *SEM3* did not have the same linear relationship for all spills. It was noted in the logbook that the ion chamber (*SEM3*) was recalibrated between run 351 and 352. The calibration after run 351 was[8]

$$10000\, SEM3 \simeq 120\, SEM4 \simeq 10^{10}\text{protons}.$$

[7]The same changes have been observed when *SEM3* is used to form the *X3l7* or *Y1R3* ratio (Figs. 4.2 and 4.3).

[8]E789 logbook, vol. 3 page. 11

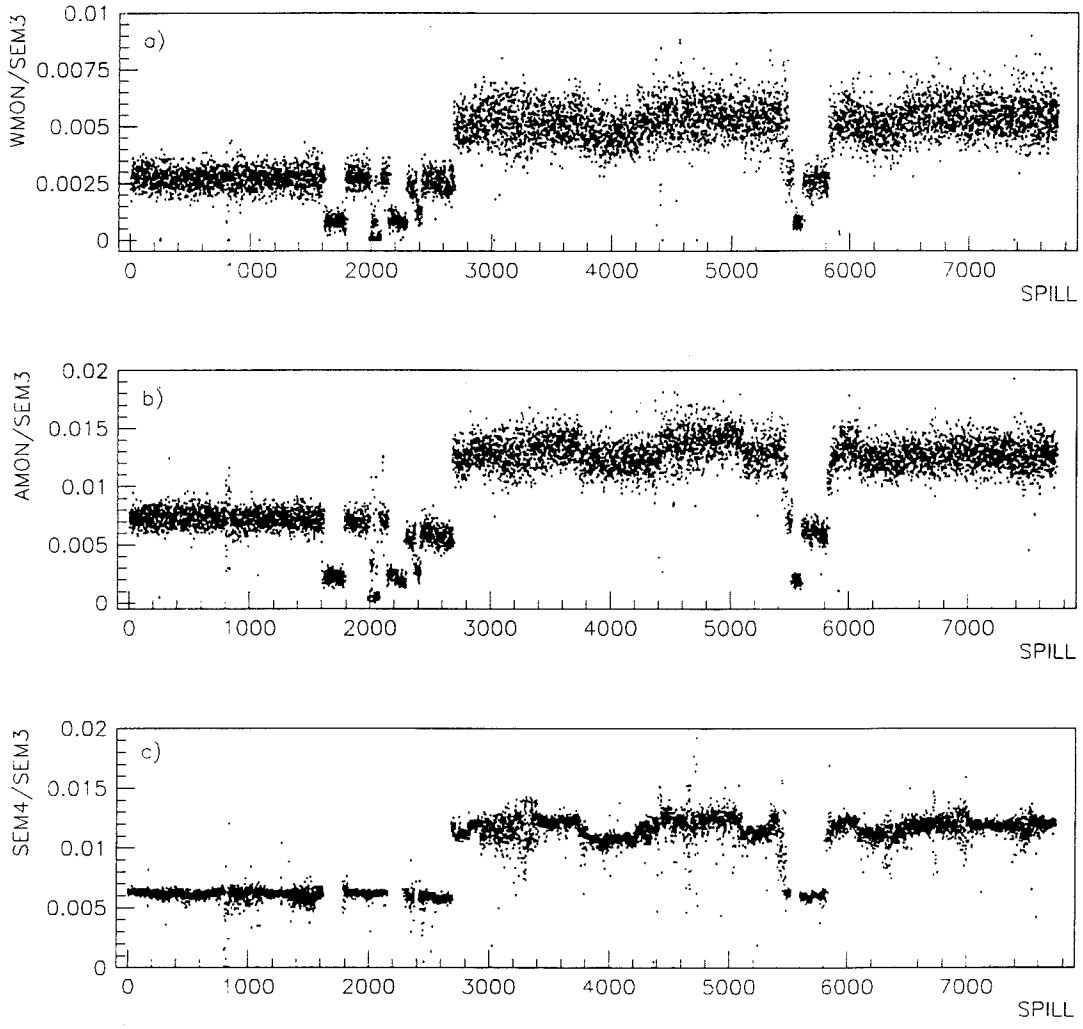

Figure 4.10: Ratios of the 90^0 scintillation telescopes and *SEM4* to *SEM3* versus spill. The same changes are observed in the three plots.

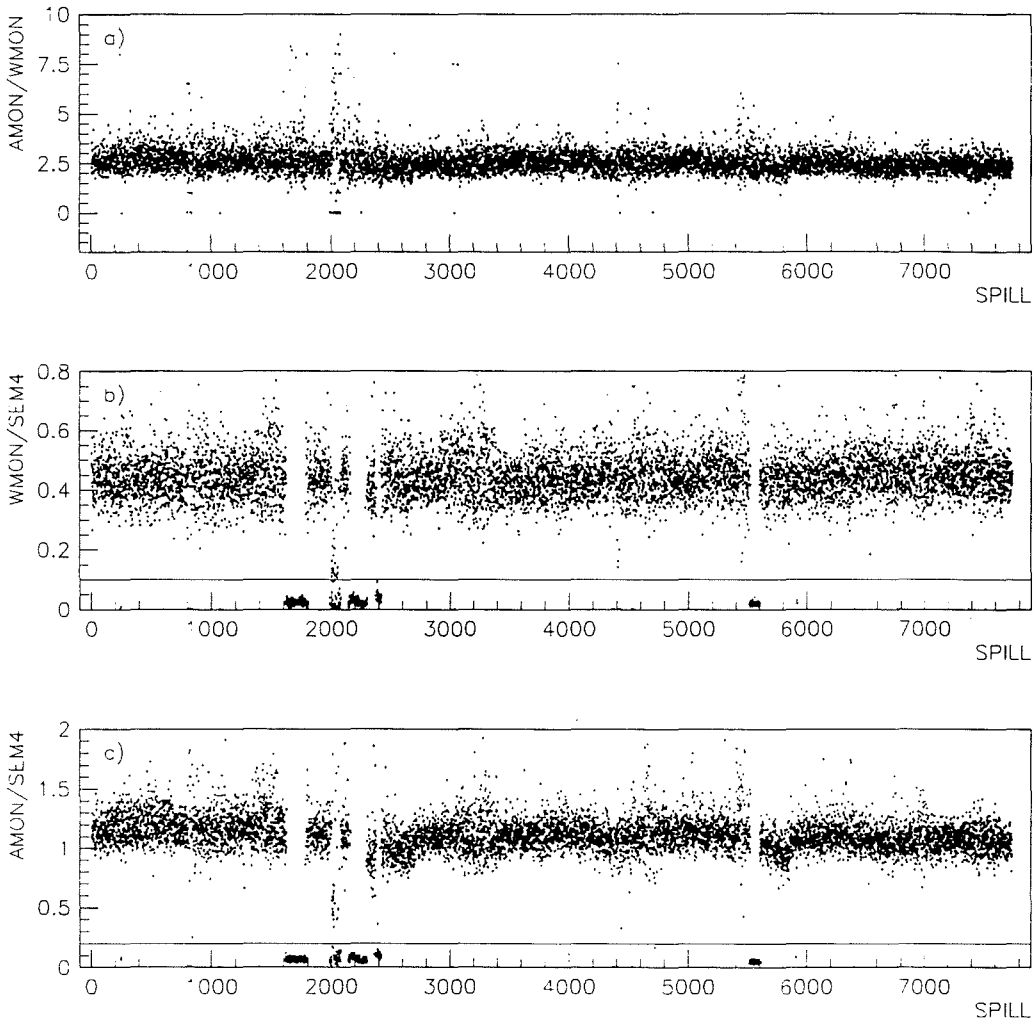

Figure 4.11: Ratios of the 90^0 scintillation telescopes and *SEM4* versus spill. Few changes are observed in these plots. Spills below the horizontal lines corresponds to spills where the beam was far away from the center of the target (see section 4.3.1.b).

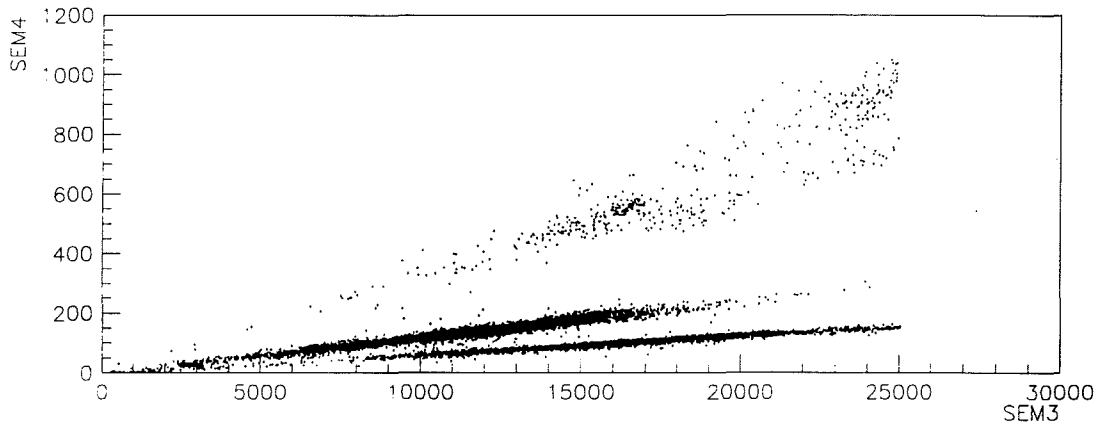

Figure 4.12: *SEM4* versus *SEM3*. *SEM3* and *SEM4* did not maintain the same linear relationship during the experiment. The reason is because the ion chamber was recalibrated in the middle of the experiment. Spills above the two lines correspond to spills where the beam was far away from the center of the target (see section 4.3.1.b).

The change in calibration of the ion chamber explains the abrupt vertical shift of the ratios formed with respect to *SEM3* (Figs. 4.2, 4.3, and 4.10). It is also the reason the data are distributed along two lines of different slopes in the plot of *SEM3* vs *SEM4* (Fig. 4.12). Those spills in Fig. 4.12 that are distributed above the two well-defined lines correspond to spills where the beam was far away from the center of the target (the sensitivity of *SEM3* to the position of the beam is studied below). The small vertical shifts observed in the *SEM3* ratios in Figs. 4.2, 4.3, and 4.10 are partly due to changes in the position of the beam.

It is important to mention that, as opposed to that at spill 2687, the jumps observed in the *SEM3* ratios at spill numbers 5656-5783 (runs 334, 350, and

351) do not correspond to actual changes in *SEM3* calibration but rather to the way numbers were assigned to each spill. Spill numbers were assigned sequentially as the data tapes were written, but the tapes were not sequentially read. The run order is displayed in Fig 4.13, where run number versus spill is shown. From the figure we can observe that the runs corresponding to spill

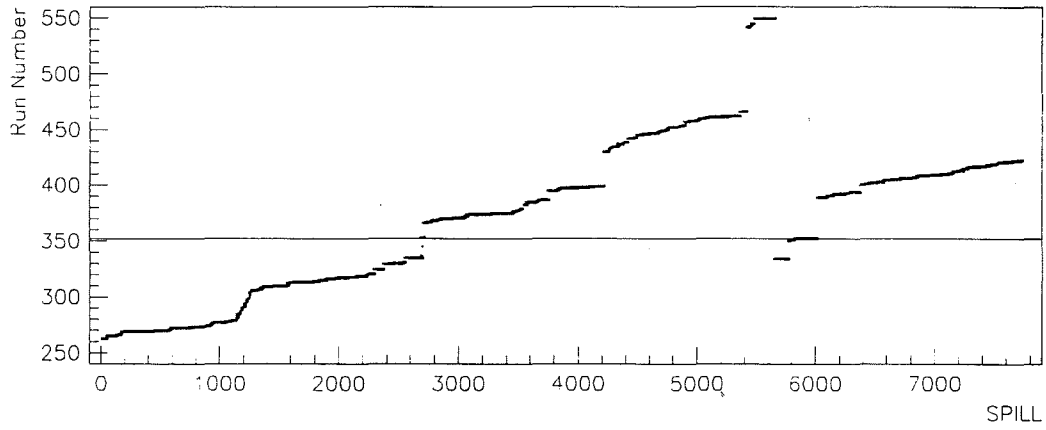

Figure 4.13: Run number versus spill number. Here we can see that consecutive runs do not have consecutive *absolute* spill number. The horizontal line corresponds to the run where the calibration of *SEM3* was performed (run 351).

numbers 5656-5783 are earlier runs than run 352 (when *SEM3* experienced the calibration change).

The intensity of the beam increased approximately 27% after run 351. The increase in the beam intensity can be observed in the histograms of *SEM4* and *AMON* (Fig. 4.14).

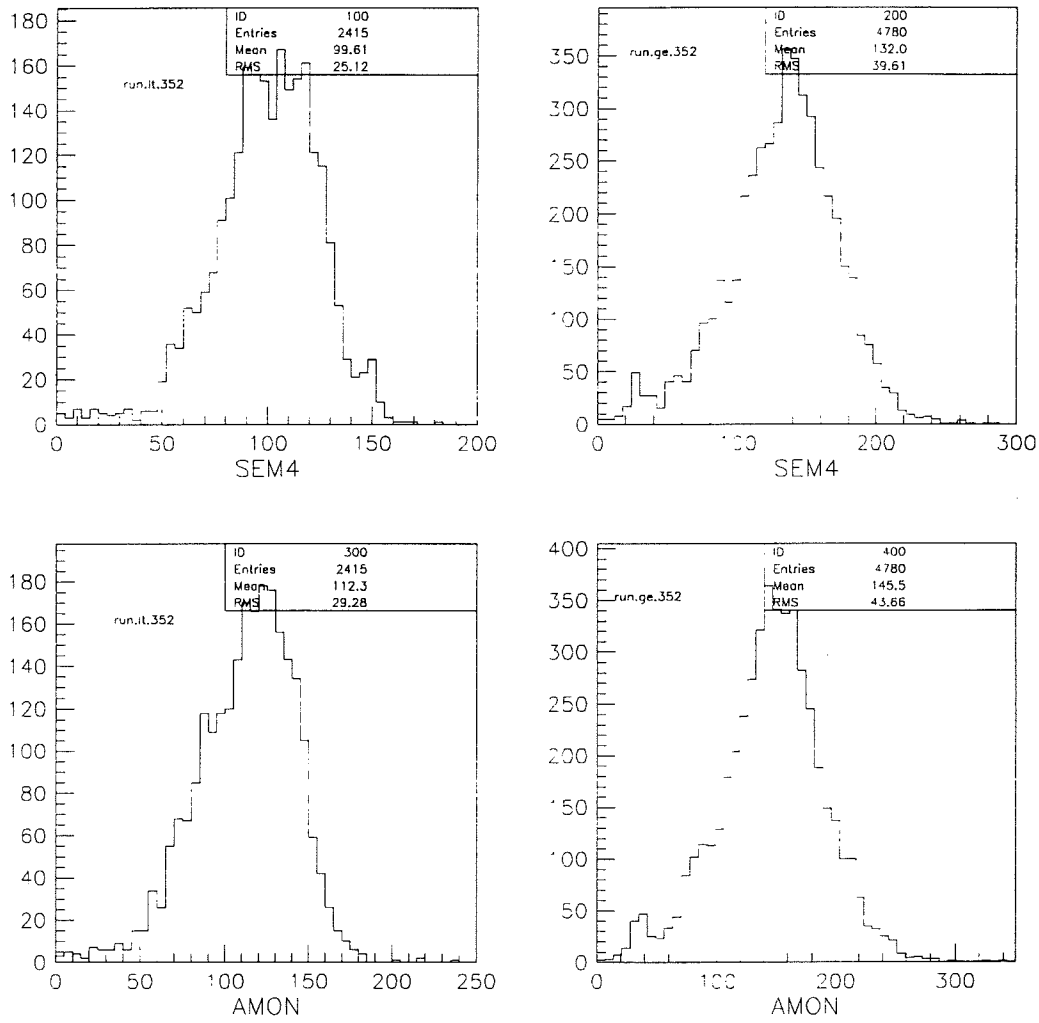

Figure 4.14: Beam intensity histograms. The intensity of the beam increased 27% after run 351.

4.3.1.b Changes in *SEM3* due to Changes in Beam Position

To look for spills with similar beam position I used the information from the hodoscope counters at station 4 (x and y). The ratios of the right and left components of the x and y hodoscopes give information about the horizontal displacement of the beam with respect to the y-z plane. For example, if the beam is displaced to the left, the left components of the hodoscopes will register more counts than the right ones, making the values of the right over left ratios smaller than one. These ratios will be greater than one when the beam is displaced to the right.

If we make a scatter plot of *Y4R/Y4L* versus *X4R/X4L*, we expect to see the data distributed along a line of positive slope. Fig. 4.15 shows the scatter plot of *Y4R/Y4L* versus *X4R/X4L* and the histograms of the *X4* and *Y4* right-left ratios. The distribution of the data in the scatter plot (along two oppositely-sloped lines) is not what is expected. The reason for this behavior is unknown. It may be due to an interchange of cabling at some point in the course of the experiment of the right and left components of the y hodoscope or to a change of the right and left components of either the x or y hodoscope into the up and down components. The behavior of the data, although unexpected, still might give information about the position of the beam, and therefore I can try to use the data to group spills with similar beam position. Using the scatter plot and the histograms of Fig. 4.15, I grouped spills with similar values of *X4R/X4L* and also similar values of *Y4R/Y4L*. The location of the beam for those spills should be almost the same. The grouping conditions are

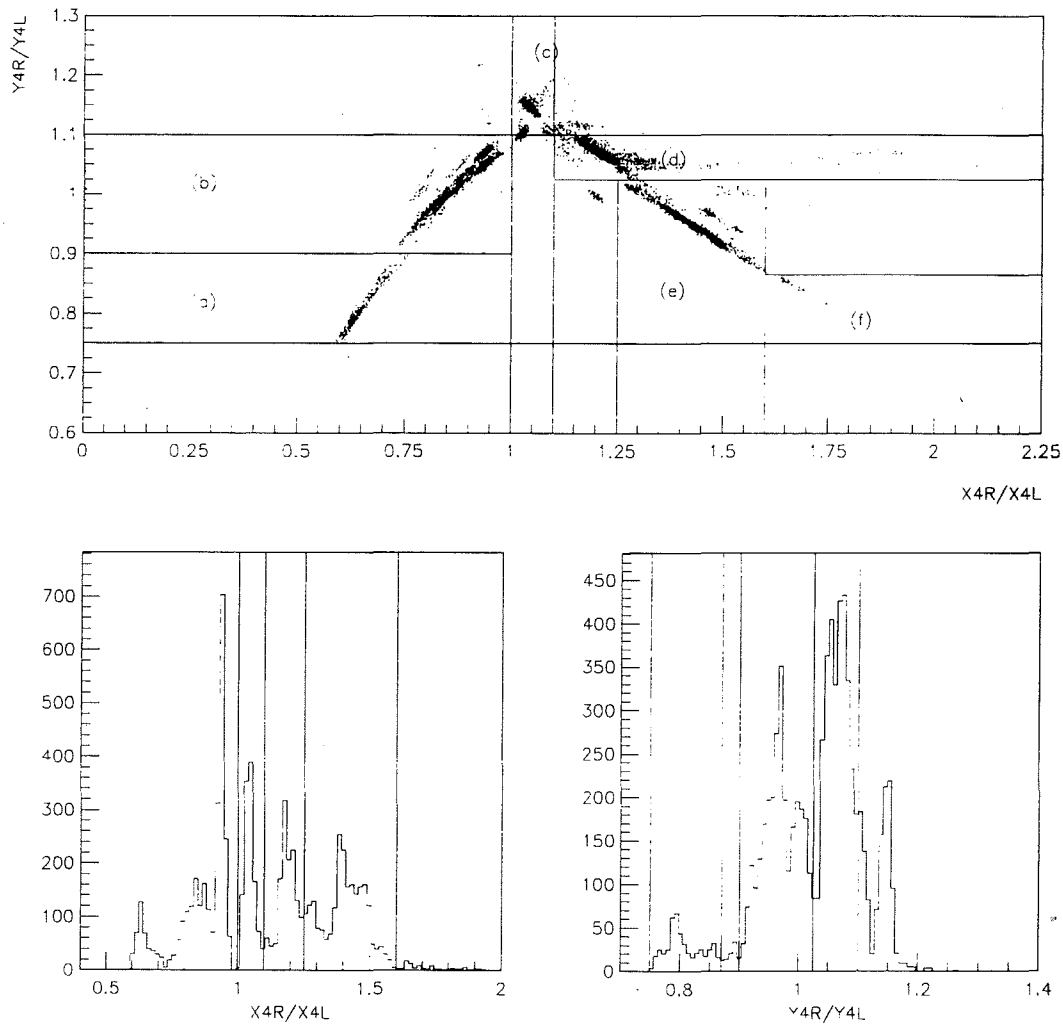

Figure 4.15: Scatter plot and histograms of *X4R/X4L* and *Y4L/Y4R*. The plots show the changes in the incident position of the beam.

listed in Table 4.3 and indicated on the scatter plot and the histograms. To

Table 4.3: Cuts defined on *X4R/X4L* and *Y4R/Y4L* to group spills with similar beam position.

Cut	*X4R/X4L* Condition					*Y4R/Y4L* Condition				
(a)	0	$<$	*X4R/X4L*	$<$	1.0	0.75	$<$	*Y4R/Y4L*	$<$	0.9
(b)	0	$<$	*X4R/X4L*	$<$	1.0	0.90	$<$	*Y4R/Y4L*	$<$	1.1
(c)	1.0	$<$	*X4R/X4L*	$<$	1.1	1.1	$<$	*Y4R/Y4L*	$<$	1.3
(d)	1.1	$<$	*X4R/X4L*	$<$	1.25	1.025	$<$	*Y4R/Y4L*	$<$	2.25
(e)	1.25	$<$	*X4R/X4L*	$<$	1.60	0.865	$<$	*Y4R/Y4L*	$<$	1.025
(f)	1.60	$<$	*X4R/X4L*	$<$	2.25	0.75	$<$	*Y4R/Y4L*	$<$	0.865

see the effect of the beam position, I plotted *Y1R3/SEM3* versus spill for each of the different beam-position cuts defined in Table 4.3 (Figs. 4.16 and 4.17). In each of these plots the values of *Y1R3/SEM3* are almost the same for each spill, suggesting that *SEM3* was sensitive to the position of the beam.

4.3.1.c Ratios of Protons Incident on Each Target

To obtain α we need to calculate the ratios of the proton flux incident on each target (Eqs. 4.2, 4.3). The ratio of number of protons incident on targets j and i is given by,

$$\frac{(N_{inc})_j}{(N_{inc})_i} = \frac{\mathrm{B}_j \times \mathrm{C}_\mathrm{B}}{\mathrm{B}_i \times \mathrm{C}_\mathrm{B}}, \tag{4.5}$$

where B_j and B_i are the total number of counts of a beam intensity monitor (*SEM3* or *SEM4*) for targets j and i and C_B is the calibration constant of that beam intensity monitor. The calibration constant cancels out if it is the same for all spills. If a beam intensity monitor had more than one calibration, the calibration constants will still cancel if the following relationship holds for

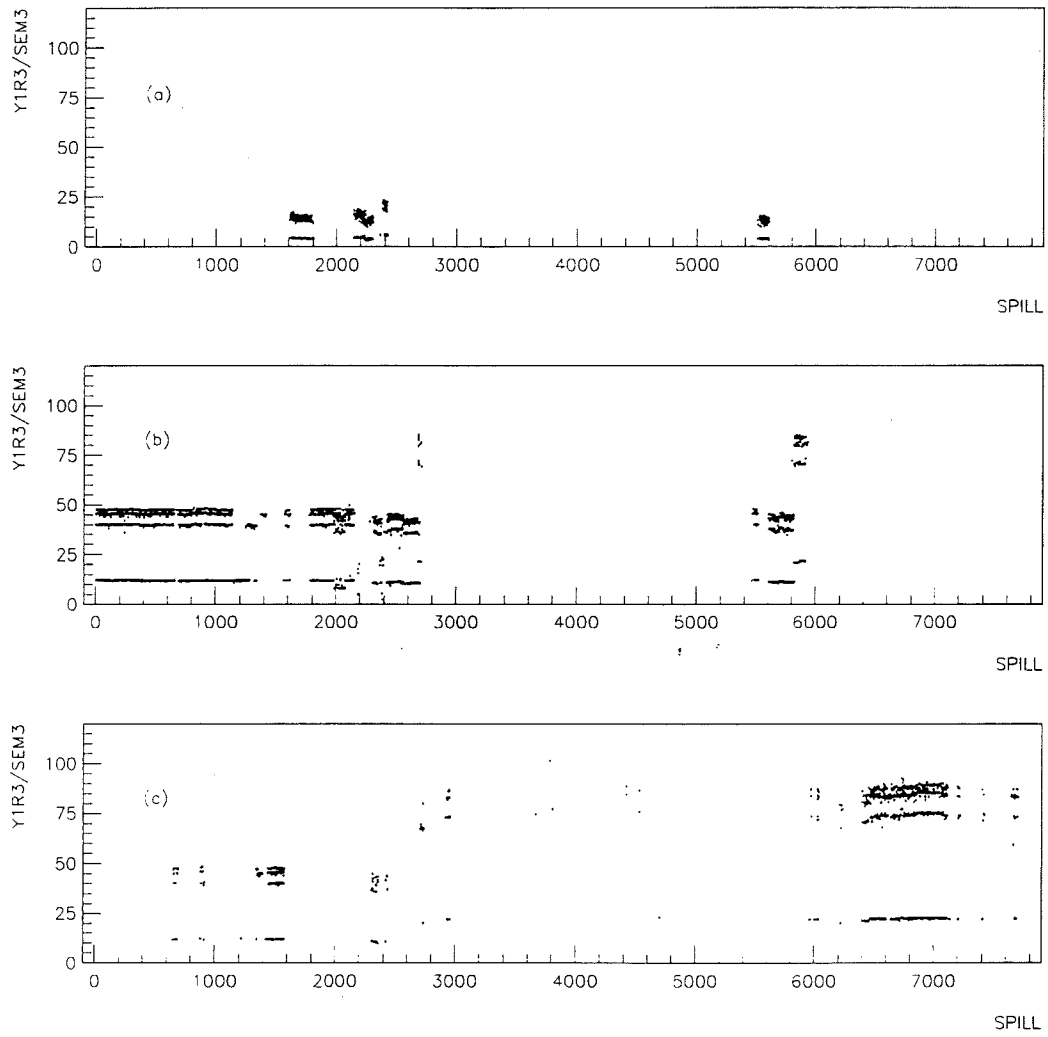

Figure 4.16: *Y1R3/SEM3* versus spill for the different cuts. Cut (a) corresponds to spills where the beam was far away from the center of the target ($AMON/SEM4 < 0.2$).

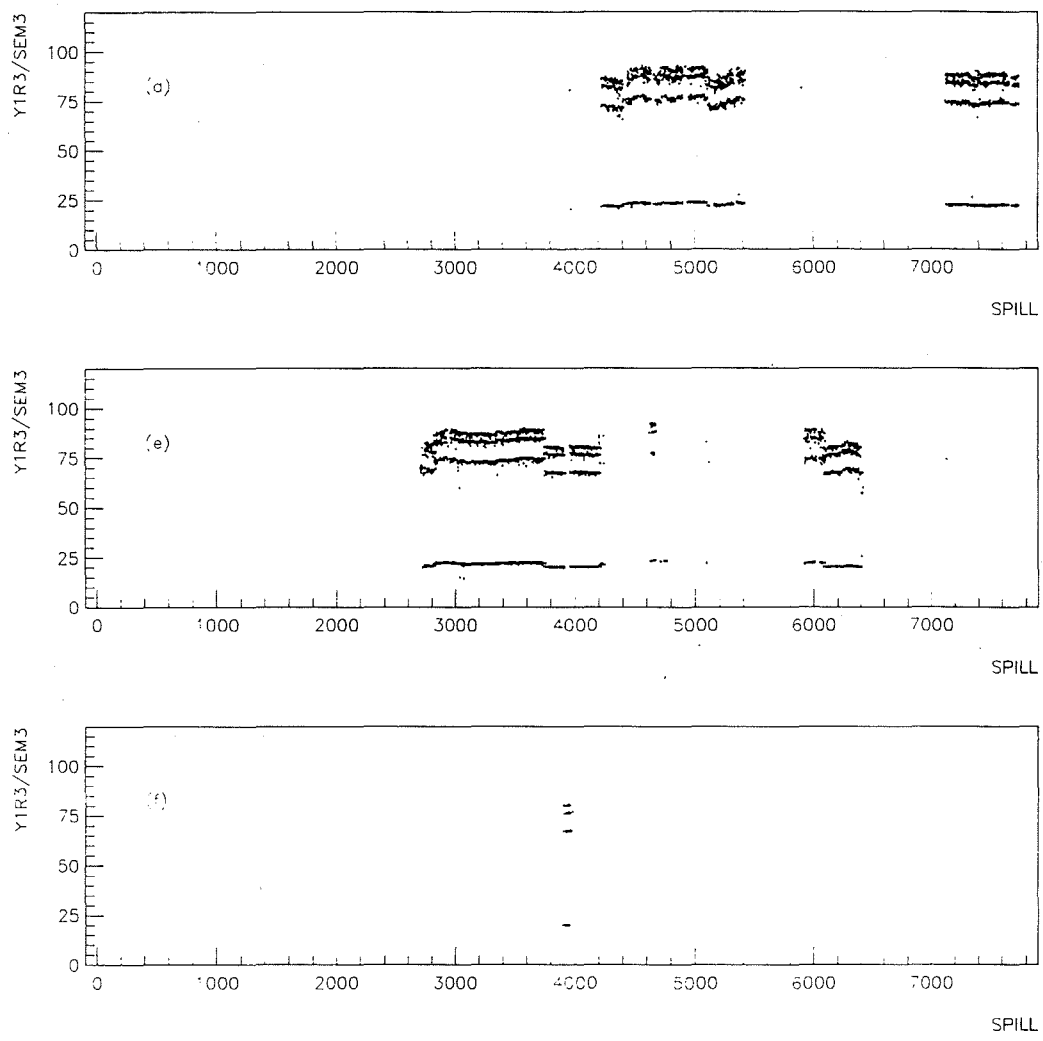

Figure 4.17: *Y1R3/SEM3* versus spill for the rest of the cuts. Although I was able to group spills with similar values in the ratio of *Y1R3/SEM3* there are still group of spills that correspond to similar beam positions but with different *Y1R3/SEM3* ratio (cut e).

all pairs of targets:

$$\frac{p_1}{q_1} = \frac{p_2}{q_2} = ... = \frac{p_n}{q_n}, \tag{4.6}$$

where p_1, p_2,..., p_n, and q_1, q_2,..., q_n are the total counts of the beam intensity monitors for targets p and q and calibrations 1, 2,..., n. Calibration constants do not cancel in any other case.

The calibration constant for *SEM4* was the same for all spills and so we do not need to consider it in the calculation of the ratios of number of protons incident on each target. However, since *SEM3* had two different calibration constants we need to find out if the relationship of Eq. 4.6 holds. Table 4.4 gives the total counts of the beam intensity monitors (*SEM3* and *SEM4*) for the two calibrations of *SEM3* and Table 4.5 gives the ratios of *SEM3* for each pair of targets. From Table 4.5 we see that the *SEM3* ratios, for each pair

Table 4.4: Total counts of the beam intensity monitors for each target.

		run $<$ 352	run $\geq$ 352
Empty	*SEM3*	1.13e7	1.37e7
	SEM4	6.96e4	1.58e5
	Spills	698	1239
W	*SEM3*	9.8e6	1.38e7
	SEM4	5.58e4	1.6e5
	Spills	594	1207
C	*SEM3*	9.51e6	1.39e7
	SEM4	5.82e4	1.61e5
	Spills	599	1194
Be	*SEM3*	8.53e6	1.31e7
	SEM4	5.23e4	1.52e5
	Spills	524	1135

Spills with *AMON/SEM4* $<$ 0.2 were excluded.

of targets and for the two calibrations, differ by up to $\approx 21\%$. Therefore to get the fraction of beam received by each target using *SEM3*, we need to take into account the relationship between the two calibrations. Table 4.6 gives the

Table 4.5: *SEM3* ratios of the number of protons incident on each target for the two calibrations of *SEM3*.

	run < 352	run ≥ 352	difference
Empty/W	1.15	0.99	13.9%
Empty/C	1.19	0.99	17.0%
Empty/Be	1.33	1.05	21.1%
W/C	1.03	0.99	3.6%
W/Be	1.15	1.05	8.4%
C/Be	1.12	1.06	4.8%

total counts of *SEM4* and *SEM3* (correcting and without correcting for the two calibrations) for each target. The beam-intensity-monitor ratios between targets are given in Table 4.7. We see that after the correction, the flux ratios given by *SEM4* and *SEM3* agree. These two independent measurements allow us to derive the systematic uncertainties in the flux-ratio determination. The final flux-ratios necessary to calculate α are given in Table 4.3.1.c. The systematic uncertainties are typically less than 1%.

The small shifts observed when ratios involving *SEM3* are plotted are mostly due to changes in the position of the beam.[9] When *SEM3* is used to calculate the fraction of beam received by each target, it is necessary to know if the sensitivity of *SEM3* to the position of the beam affected significantly the ratios of the beam received by each target. Table 4.9 gives the total *SEM3* for

[9] *SEM3* is the only beam intensity monitor sensitive to the position of the beam.

Table 4.6: Total *SEM3* and *SEM4* received by each target.

	SEM3	*SEM3* (corrected)	*SEM4*
Empty	2.5*e*7	3.7*e*7	2.28*e*5
W	2.36*e*7	3.57*e*7	2.16*e*5
C	2.33*e*7	3.55*e*7	2.19*e*5
Be	2.16*e*7	3.31*e*7	2.04*e*5

Table 4.7: Beam-intensity-monitor ratios between targets given by *SEM3*, *SEM3*-corrected, and *SEM4*.

	SEM3	*SEM3*(correct.)	*SEM4*
Empty/W	1.059	1.036	1.056
Empty/C	1.073	1.042	1.041
Empty/Be	1.157	1.118	1.065
W/C	1.093	1.079	1.059
W/Be	1.013	1.006	0.986
C/Be	1.079	1.073	1.074

Table 4.8: Beam intensity ratios.

Empty/W	Empty/C	Empty/Be
$1.05 \pm 0.95\%$	$1.04 \pm 0.05\%$	$1.09 \pm 2.35\%$

W/C	W/Be	C/Be
$1.07 \pm 0.95\%$	$1.00 \pm 0.95\%$	$1.07 \pm 0.05\%$

each target correcting and without correcting for the small changes of *SEM3*. Since in the table we observe that in both cases, the percentages of beam received by each target agree within $\approx 0.5\%$, we do not need to consider the changes in *SEM3* due to the position of the beam in calculating the ratios of proton flux incident on each target.

Table 4.9: Total *SEM3* received by each target after run 351.

	SEM3		*SEM3* (corrected)		differences (%)
Empty	1.40*e*7	25.0%	1.33*e*7	24.9%	0.2
W	1.44*e*7	25.7%	1.37*e*7	25.7%	0.5
C	1.43*e*7	25.5%	1.36*e*7	25.5%	0.1
Be	1.34*e*7	24.0%	1.28*e*7	24.0%	0.4

The corrections for the small changes observed in *SEM3* due to the change in the position of the beam are also included. The differences are not significantly important.

4.3.2 Beam Duty Factor

The number of accidental coincidences[10] increases linearly with the intensity of the beam. Duty factor is defined as the ratio of working time to total time for an intermittently operating device. It is a quantity that gives information about how the values of a changing signal (in our case, the number of protons per bucket in a spill) are distributed around their mean. Duty factor correlates with inefficiencies in detectors due to increases in the number of accidental coincidences. In the off-line analysis, spills with low duty factor are discarded

[10]By accidental coincidences is meant the detection of two particles coming from different interactions but arriving at the detectors at the same time.

to reduce the presence of background reactions and thus increase the signal to background ratio.

The variance gives information about how a random variable is distributed around its mean value. Therefore, we can get an expression for duty factor from the expression for the variance of a random variable. The variance of a random variable is defined as:

$$\mathrm{var}(x) = \frac{1}{N}\sum_{j=1}^{N} x_j^2 - \frac{1}{N^2}\Big(\sum_{j=1}^{N} x_j\Big)^2. \tag{4.7}$$

For a uniform distribution (e.g. protons evenly distributed in the buckets of a spill) the value of the variance is zero, therefore,

$$\frac{1}{N}\sum_{j=1}^{N} x_j^2 = \frac{1}{N^2}\Big(\sum_{j=1}^{N} x_j\Big)^2, \tag{4.8}$$

or

$$\frac{\left(\sum_{j=1}^{N} x_j\right)^2}{N\sum_{j=1}^{N} x_j^2} = 1. \tag{4.9}$$

For non-uniform distributions the left-hand side of Eq. 4.9 is less than 1. From Eq. 4.9 duty factor is defined as

$$DF = \frac{\left(\sum_{j=1}^{N} x_j\right)^2}{N\sum_{j=1}^{N} x_j^2}. \tag{4.10}$$

We can see that the value of DF is one for a uniform distribution and less than one for any other distribution.

Experimentally, duty factor can be measured by calculating the ratio of the product of singles rates over accidental rates observed in two independent counters. By independence I mean that the counts registered in one counter do not affect the counts registered in the other one. To see the equivalence

between the theoretical definition and the experimental calculation of duty factor I need to introduce some statistical quantities. The first one is the number of counts in a spill registered by counter i:

$$c_i = \xi_i \sum_{j=1}^{N} n_j, \tag{4.11}$$

where n_j is the number of interactions occurring in bucket j and ξ_i is the probability for counter i to count per interaction. The number of accidental accidental coincidences in a spill on two widely separated counters $(1,2)$ depends on the product of the probabilities for each counter:

$$c_{12}^{\text{acc}} = \xi_1 \xi_2 \sum_{j=1}^{N} {n_j}^2. \tag{4.12}$$

The number of real coincidences in a spill, that is, the number of particle-pairs coming from the same interaction, is

$$c_{12}^{\text{real}} = \xi_{12} \sum_{j=1}^{N} n_j, \tag{4.13}$$

where ξ_{12} is the probability of observing two particles coming from the same interaction. From Eq. 4.12 and 4.13 we see that accidental coincidences vary as the square of the intensity and real coincidences vary linearly with the intensity. Considering the ratio of single counts and accidental coincidences in each spill, we have

$$R = \frac{c_1 c_2}{c_{12}^{\text{acc}}} = \frac{(\sum_{j=1}^{N} n_j)^2}{\sum_{j=1}^{N} n_j^2}. \tag{4.14}$$

In a perfect spill the number of interactions occurring per bucket is constant (i.e. $n_j = n$ for $j = 1, 2, ..., N$) and thus the ratio

$$R = \frac{(nN)^2}{Nn^2} = N \tag{4.15}$$

gives the number of buckets in the spill. Using the above definition of R, we now can express duty factor as

$$DF = \frac{R}{N} = \frac{c_1 c_2}{N c_{12}^{acc}} = \frac{(\sum_{j=1}^{N} n_j)^2}{N \sum_{j=1}^{N} n_j^2}. \tag{4.16}$$

This is the same expression as in eq. 4.10. From the above equation we see that DF is independent of the intensity of the beam. For a perfect spill the value of DF is 1, but due to fluctuations in the beam transfer process DF is typically smaller than 1. For example, in the case of spill with half of its buckets empty and the other half each containing n protons, the value of DF is

$$DF = \frac{(nN/2)^2}{N(n^2N/2)} = \frac{1}{2}. \tag{4.17}$$

In the experiment we created the coincidence signal by performing a logical *AND* operation between signals from two approximately uncorrelated hodoscope counters, *X3L7* and *Y1R3*. The coincidence was labeled in the scalers as *X3L7Y1R3*. *X3L7Y1R3* was generated in two different modes. To distinguish the modes I will add the subscript "in" and "out" to the *X3L7Y1R3* scaler. $X3L7Y1R3_{\text{in}}$ summed the coincidences observed from the same bucket, while $X3L7Y1R3_{\text{out}}$ summed the coincidences observed from two different buckets (one of the signals delayed by three buckets). $X3L7Y1R3_{\text{in}}$ had real as well as accidentals coincidences in it.

In the off-line analysis, duty factor was formed as

$$DF_{\text{exp}} = \frac{X3L7 \times Y1R3 \times 256}{X3L7Y1R3 \times N_o}. \tag{4.18}$$

The factor of 256 appears because the scalers *X3L7* and *Y1R3* were each prescaled by a factor of 16. N_o, the number of buckets in a spill, is not

necessarily constant. In the analysis I have used $N_o = 10^9$ because it is an accurate approximation of the number of buckets per spill. $DF_{\rm exp}$ versus spill is plotted for both coincidence scalers in Fig. 4.18. The values of $DF_{\rm exp}$ found using the in-time scaler are rather low when comparing these values with the ones found in the previous experiment, E772 [22] (Fig. 4.19). The reason is that the in-time coincidence scaler had many reals in it, reducing the value of $DF_{\rm exp}$. The out-of-time plot, however, gives values of $DF_{\rm exp}$ greater than one. A value of the out-of-time $DF_{\rm exp}$ greater than one is possible if there is a negative correlation in the intensity of the buckets put in coincidence. For example, the out-of-time $DF_{\rm exp}$ could be infinite if the protons in a spill occupied only the even or only the odd buckets, since in this case the coincidence scaler $X3L3Y1R3_{\rm out}$ will be zero (Eq. 4.18).

To calculate DF using the in-time coincidence scaler we need to correct for the real coincidences included in the in-time coincidence scaler. We can express $DF_{\rm exp}$ as

$$DF_{\rm exp} = \frac{c_1 c_2}{N_0(c_{12}^{\rm acc} + c_{12}^{\rm real})} = \frac{\xi_1\xi_2(\sum_{j=1}^{N_0} n_j)^2}{N_0(\xi_1\xi_2 \sum_{j=1}^{N_0} n_j^2 + \xi_{12} \sum_{j=1}^{N_0} n_j)}. \qquad (4.19)$$

By taking the inverse of the above equation we can separate the real and accidental contributions:

$$\frac{1}{DF_{\rm exp}} = \frac{N_0 c_{12}^{acc}}{c_1 c_2} + \frac{N_0 c_{12}^{real}}{c_1 c_2} = \frac{N_0 \sum_{j=1}^{N_0} n_j^2}{(\sum_{j=1}^{N_0} n_j)^2} + \frac{\xi_{12} N_0}{\xi_1\xi_2 \sum_{j=1}^{N_0} n_j}. \qquad (4.20)$$

The first term on the right-hand side of equation 4.20 is due only to accidentals and is independent of the intensity of the beam. We recognize it as the inverse of duty factor (Eq. 4.16). The second term is due to reals and varies inversely with the spill intensity. Both terms depend linearly on the number of buckets

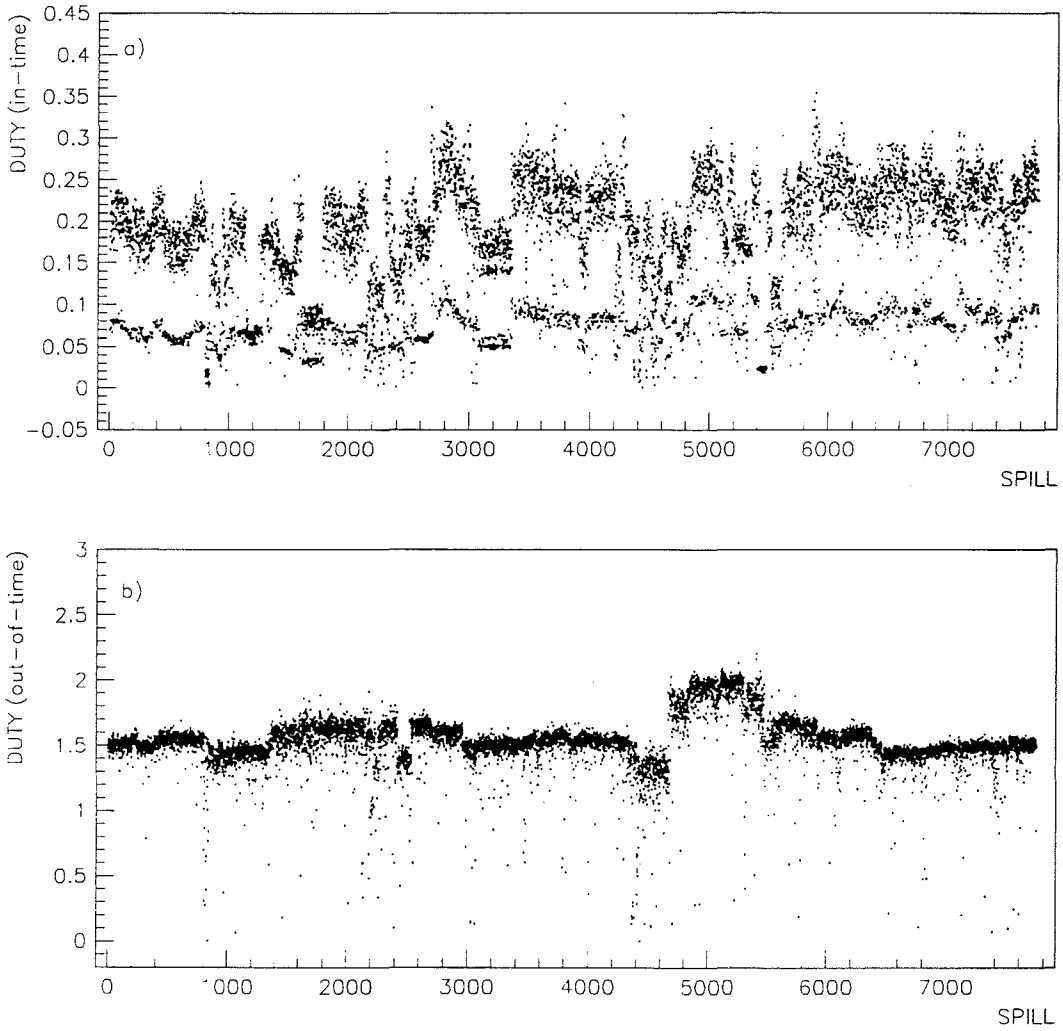

Figure 4.18: Dutv factor versus spill for the in-time and out-of-time scalers. The out-of-time F presents a value greater than one.

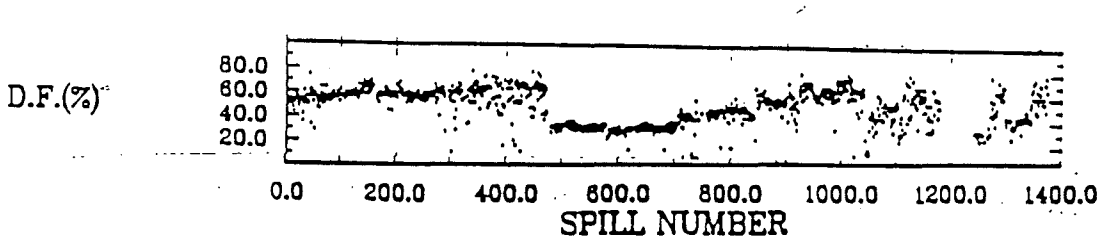

Figure 4.19: Duty factor versus spill in E772.[22].

per spill, N_0, a number that is not exactly constant but typically very close to 10^9. Eq. 4.20 can be expressed as:

$$\frac{1}{DF_{\rm exp}} = a_0 + \frac{a_1}{\rm I}, \tag{4.21}$$

where I is the intensity of the beam. Plotting $1/DF_{\rm exp}$ versus $1/Y1R$ (Fig. 4.20), we observe the expected linear dependence of Eq. 4.21. Using Eq. 4.20 we can calculate DF by subtracting, for each target, the term proportional to the real coincidences. The term corresponds to the slopes of the plots in Fig. 4.20. The slope values, a_1, are different for each target because a_1 is a value that depends on the real coincidences and real coincidences have a target dependence. DF can then be expressed as,

$$a_0^{-1} = DF = \frac{c_1 c_2}{N c_{12}^{acc}} = \left(\frac{1}{DF_{\rm exp}} - \frac{N c_{12}^{real}}{c_1 c_2} \right)^{-1} = \left(\frac{1}{DF_{\rm exp}} - \frac{a_1}{\rm I} \right)^{-1}. \tag{4.22}$$

The fits are shown in Fig. 4.21. The fit parameters are shown on the figure and given in Table 4.10. The values of the parameters changed depending on the number of bins defined. To get the fit parameters for each figure I chose the binning which gave the same duty factor at infinite intensity for

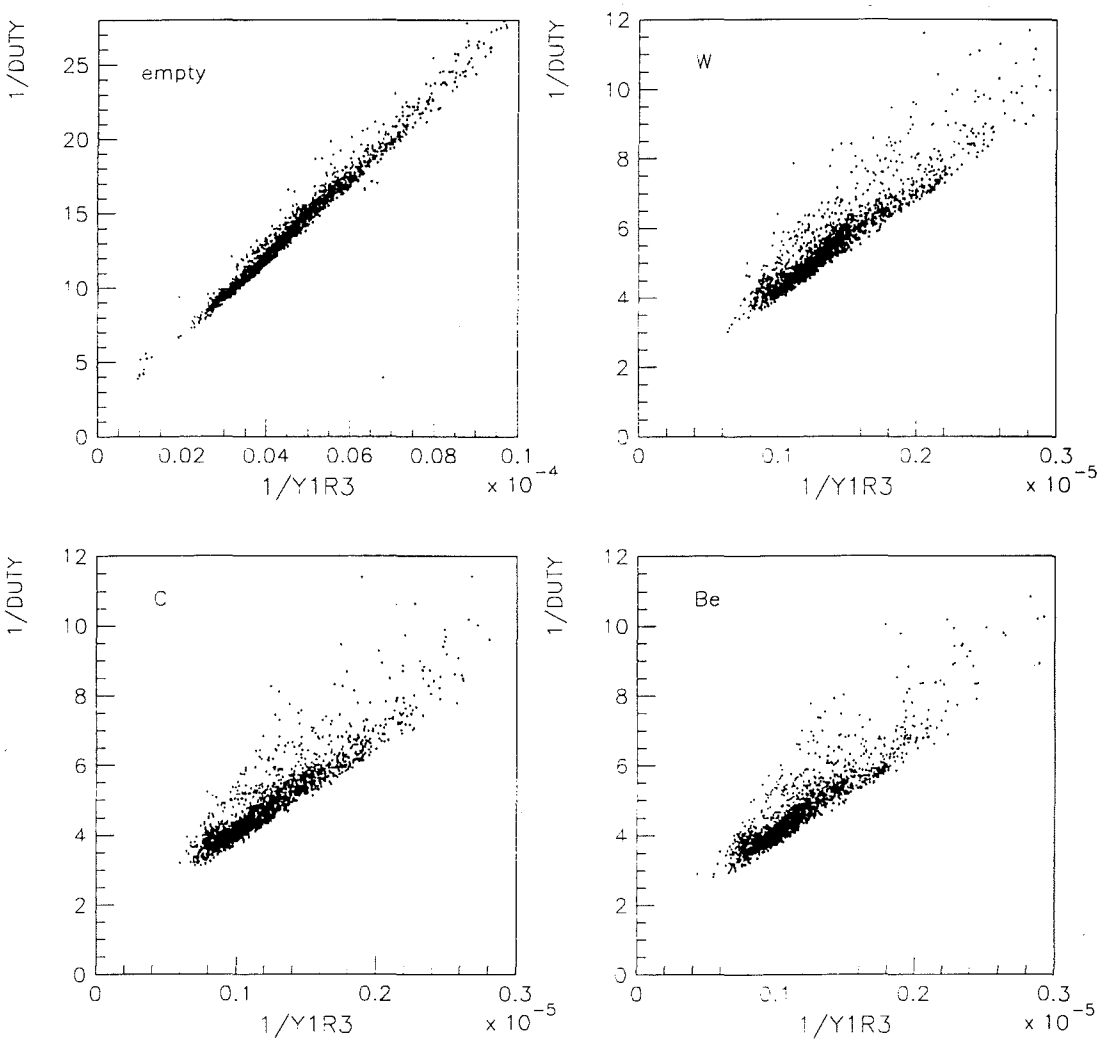

Figure 4.20: $1/DF_{\text{exp}}$ versus $1/Y1R3$ for all targets. For the (a) empty, (b) tungsten, (c) carbon, and (d) berylium target. Spills with $AMON/SEM4 < 0.2$ were excluded.

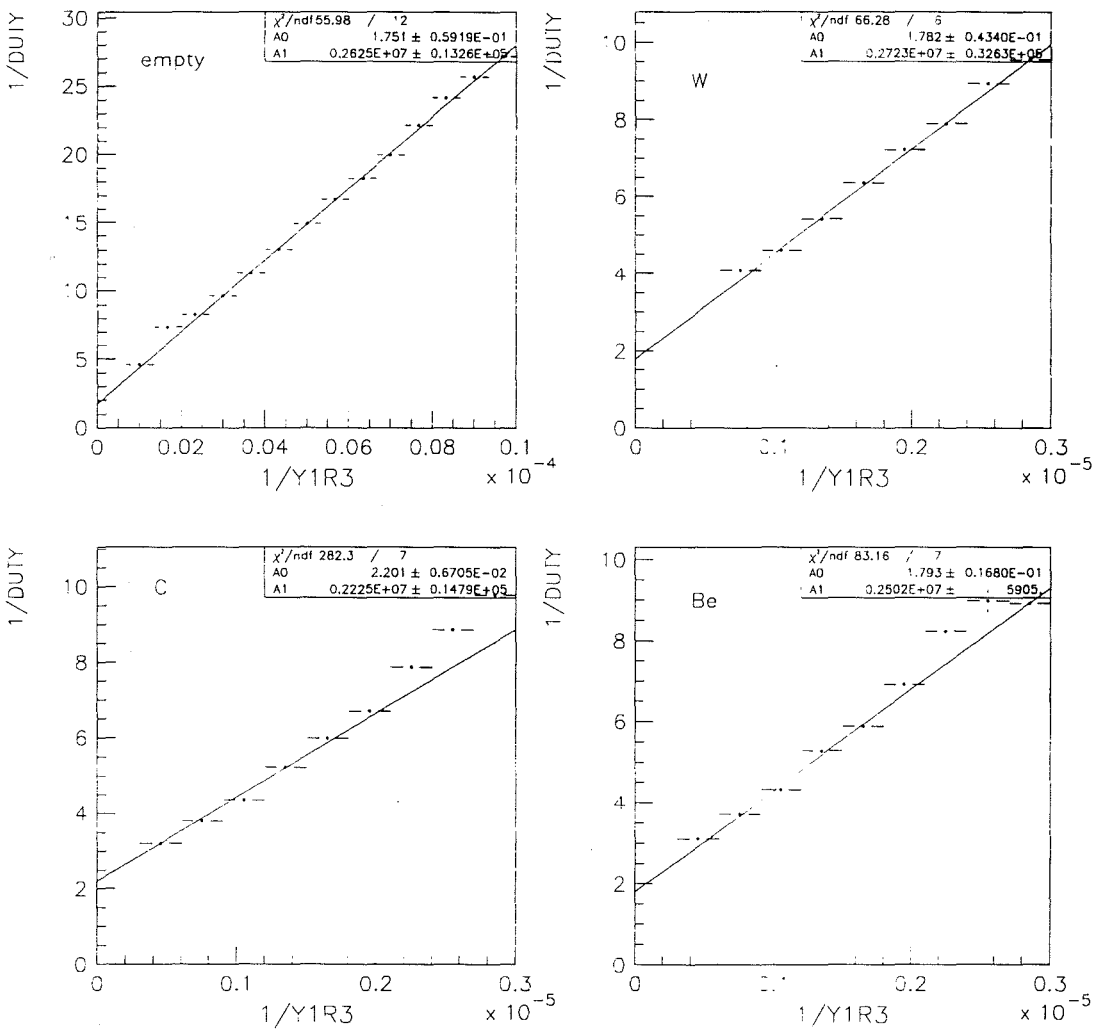

Figure 4.21: Fits of $1/DF_{\rm exp}$ versus $1/Y1R3$ for all targets. The slope of the plots are proportional to the number of reals in the $X3L7Y1R3_{\rm in}$ scaler for each target.

Table 4.10: Fit parameters for the calculation of duty factor.

Target	a_0	a_1	bins
Be	1.78 ± 0.04	$2.52 \times 10^6 \pm 3 \times 10^4$	10
C	1.76 ± 0.04	$2.57 \times 10^6 \pm 3 \times 10^4$	10
W	1.78 ± 0.04	$2.73 \times 10^6 \pm 3 \times 10^4$	10
Empty	1.74 ± 0.06	$2.63 \times 10^6 \pm 10^4$	15

The fit parameters are taken from Fig. 4.21.

all the targets. The reason is that at infinite intensity the number of real coincidences is negligible when compared with the accidental coincidences (see for example Eq. 4.19) and therefore at infinite intensity we do not need to correct for the reals to obtain the duty factor of the beam. Since duty factor is target independent it should be the same for all targets (i.e. the value of a_0, in Table 4.10 should be the same). In Table 4.10 we see that the term proportional to the number of reals increases with target atomic weight. By plotting $(1/DF_{\rm exp} - a_1/Y1R3)$ versus $1/Y1R3$ we can obtain duty factor as expressed in Eq. 4.22. Fig. 4.22 shows the distribution of the inverse of DF versus the inverse of intensity $(1/Y1R3)$ calculated by subtracting the reals from $DF_{\rm exp}$. The scatter plots have almost the same distribution for the three targets. The distribution for the empty target has a larger RMS. Also we see that in the correction made to get rid of the reals some spills have a duty factor greater than one. The histograms of DF for all targets are shown in Fig. 4.23. Here we see that the mean duty factor is the same for all targets. $DF_{\rm exp}$, corrected for reals, versus spills is shown in Fig. 4.24. The figure has a mean duty factor of 0.59, similar to the value $\simeq 0.55$ obtained in E772 (see

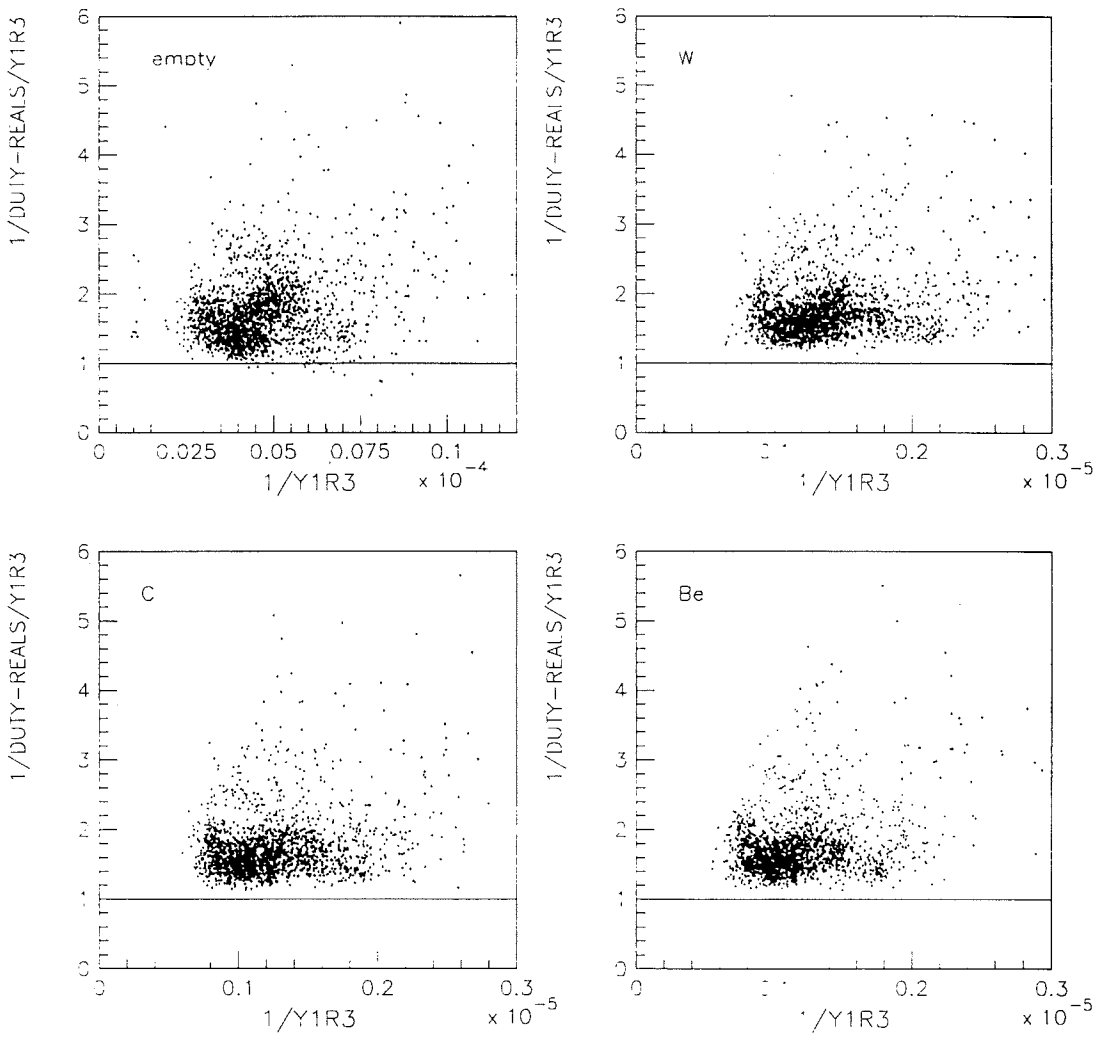

Figure 4.22: Distribution of the inverse of duty factor for all targets. The targets are: (a) the empty, (b) tungsten, (c) carbon, and (d) beryllium target. Spills with *AMON/SEM4* < 0.2 were excluded. The line has been added because it corresponds to the ideal case of a duty factor equal one and also to observe that we were able to get rid of the real coincidences present in DF_{exp}.

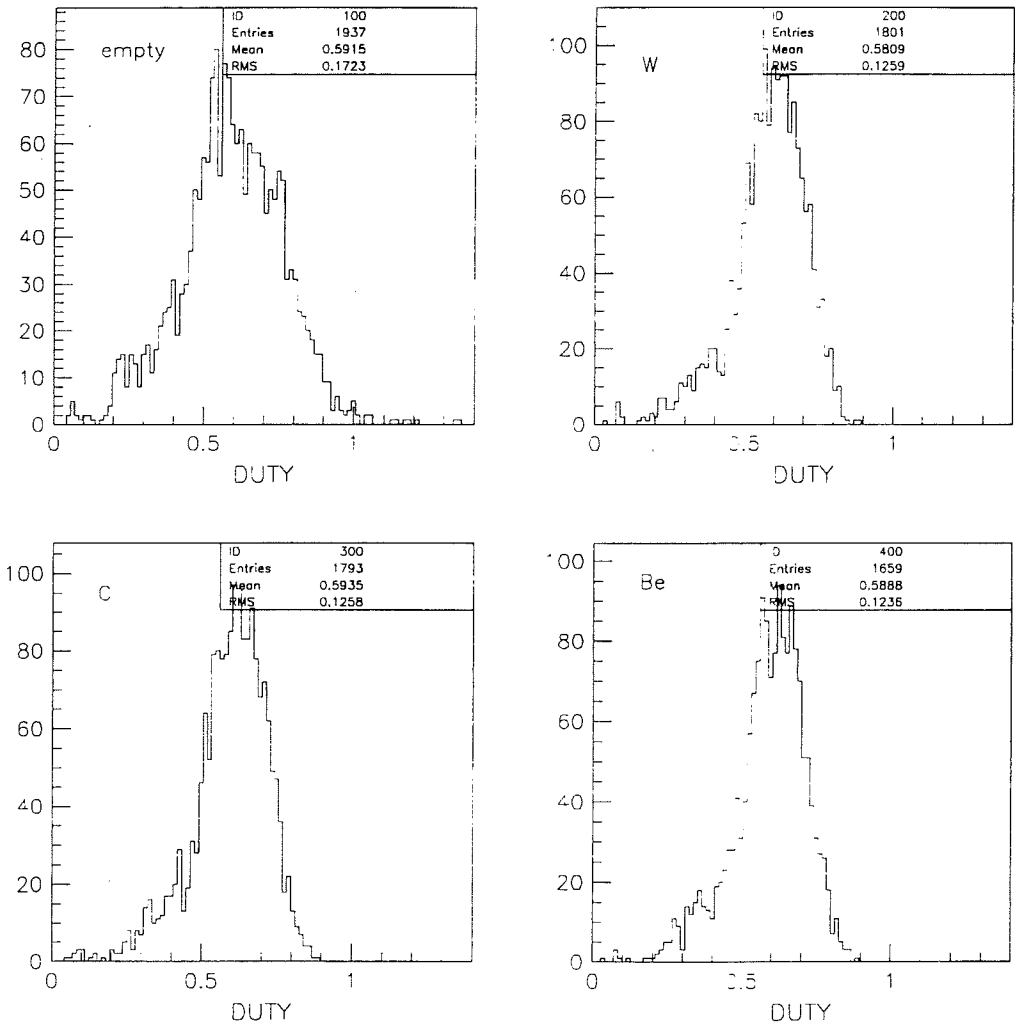

Figure 4.23: Duty factor histograms for all targets. Spills with *AMON/SEM4* < 0.2 were excluded. The distribution of duty factor is almost the same for the three targets, Be, C, and, W.

Fig.4.19 [22]).

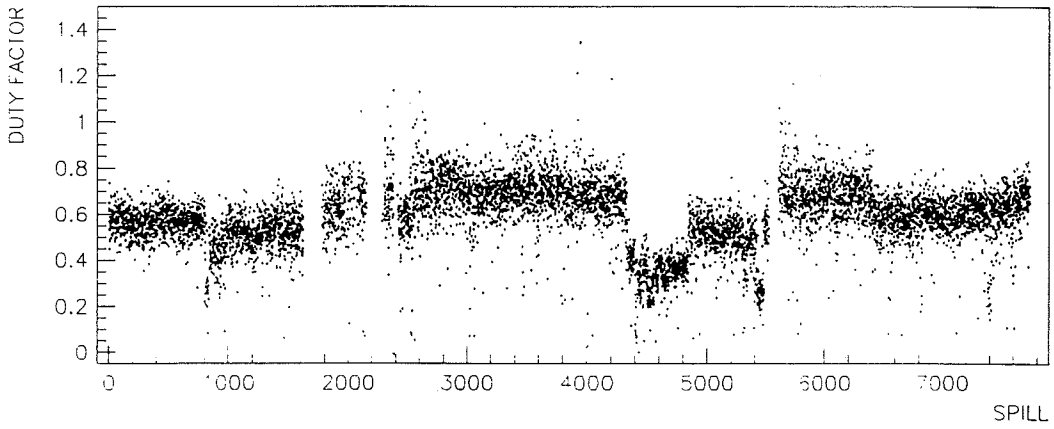

Figure 4.24: Duty factor versus spill. Here I show the duty factor where the real coincidences present in DF_{in} have been removed.

Chapter 5
CONCLUSIONS

A detailed explanation and discussion of the scaler analysis performed on beam and apparatus monitors for the study of the nuclear dependence of J/ψ for values of x_F near zero has been presented. The analysis has been carried out on 7733 spills using PAW and an n-tuple file that contained the values of the scalers for every spill. The purpose of the scaler analysis was to filter out spills with problems that could reduce the quality of the data for the third-pass analysis, and to choose for the third-pass analysis, among the redundant scalers defined in the experiment, the more reliable ones.

The scalers used to know which target was in the beam were *TARGET* and *ME6COM*. We have found that target identification scalers were very reliable. Since the *TARGET* scaler was unplugged for more than 1200 spills we used the other target scaler, *ME6COM*, to separate spills from different targets.

The scalers used to monitor live time were *SEM3*, *AMON*, *WMON*, and *TFI*. Live time scalers agreed within 3%. The scaler that gives a more accurate value of live time is *AMONSB/AMON*. Live time was target independent. Therefore in the calculation of the cross-section ratios live time cancels out.

Magnet currents were very stable through the experiment. The current varied less than 0.06% for *SM12* and less than 0.1% for *SM3*.

The scalers used to calculate the beam flux were *SEM3* and *SEM4*. *SEM3*

had two different calibrations. *SEM3* was also sensitive to the position of the beam. To calculate the incident beam-flux ratios for the different targets using *SEM3* we need to correct for the changes in the calibration of *SEM3*. The systematic uncertainties in the determination of the flux-ratios are typically less than one.

To calculate duty factor two coincidence scalers were defined. $X3L7Y1R3_{\rm in}$ summed the coincidence signals observed from the same bucket. $X3L7Y1R3_{\rm out}$, summed the coincidence signals observed from two different buckets. We found the presence of many reals in the coincidence scaler, $X3L7Y1R3_{\rm in}$. Those reals reduced the apparent duty factor. The buckets put in coincidence to form the $X3L7Y1R3_{\rm out}$ were negatively correlated in intensity. Manipulating the data, we succeeded in subtracting the real coincidences from the in-time coincidence scaler, and thus we were able to get duty factor for each spill. The mean duty factor finally obtained was similar to the one obtained in the previous experiment E772.

The results of the experiment have already been published and can be found in [23]. We observe a nuclear suppression of the J/ψ production cross section in heavy targets that increases as x_F becomes negative. Nuclear suppression has also been observed in ψ' and Υ production [14, 24] but has not been found in the production of neutral D mesons [25]. The absence of nuclear suppression in neutral D meson production suggests that the nuclear dependence observed in charmonium production is probably not the result of nuclear modification of the gluon structure functions or other initial-state effects. The stronger suppression observed as x_F becomes negative can be explained as a result of

the dissociation of the $c\bar{c}$ due to other comoving partons, forming, for example, D mesons.

REFERENCES

[1] Fermilab E789 proposal, co-spokesmen: D. M. Kaplan and J. C. Peng (1988).

[2] M. Gell-Mann, Phys. Lett. **8**, 214 (1964); G. Zweig, CERN Report 8419/Th412 (1964).

[3] M. Breidenbach *et al.*, Phys. Rev. Lett. **23**, 935 (1969).

[4] J. J. Aubert *et al.*, Phys. Rev. Lett. **33**, 1404 (1974).

[5] J. E. Augustin *et al.*, Phys. Rev. Lett. **33**, 1406 (1974).

[6] B. J. Bjorken and S. L. Glashow, Phys. Lett. **11**, 255 (1964).

[7] B. J. Bjorken, J. Iliopoulos, and L. Maiani, Phys. Rev. **D2**, 1285 (1970).

[8] CDF Collaboration, F. Abe *et al.*, Phys. Rev. Lett. **74**, 2626 (1995); D0 Collaboration, S. Abachi *et al.*, Phys. Rev. Lett. **74**, 3632 (1995).

[9] S. D. Drell and T. -M. Yan, Phys. Rev. Lett. **25**, 316 (1970); I. R. Kenyon, Rep. Prog. Phys., **45**, 1261 (1982).

[10] J. J. Aubert *et al.*, Phys. Lett. **123B**, 275 (1983).

[11] R. P. Bickerstaff, M. C. Birse, and G. A. Miller, Phys. Rev. **D33**, 3228 (1986).

[12] R. Baier and R. Rückl, Z. Phys. **C 19**, 251 (1983); V. Barger, W. Y. Keung and R. J. N. Phillips, Z. Phys. **C 6**, 169 (1980).

[13] M. S. Kowitt, Ph. D. thesis, University of California, Berkeley (1992); M. S. Kowitt, *et al.*, Phys. Rev. Lett. **72**, 1318 (1994).

[14] D. M. Alde, *et al.*, Phys. Rev. Lett. **66**, 133 (1991).

[15] Y. B. Hsiung *et al.*, Phys. Rev. Lett. **55**, 457 (1985); J. A. Crittenden *et al.*, Phys. Rev. **D34**, 2584 (1986).

[16] J. C. Gursky, H. Baer, F. F. Flick, and D. Gallegos, Nucl. Instrum. Methods **A282**, 62 (1989).

[17] R. Gray and J. P. Rutherfoord, Nucl. Instrum. Methods **A244**, 440 (1986).

[18] Y. B. Hsiung, Ph. D. thesis, Columbia University (1986).

[19] J. A. Crittenden *et al.*, IEEE Trans. Nucl. Sci. **NS-31**, 1028 (1984).

[20] R. E. Plaag and J. P. Rutherfoord, Nucl. Instrum. Methods **A273**, 177 (1986).

[21] R. Brun, O. Couet, C. Vandoni, P. Zanarini. *PAW - Physics Analysis Workstation.*, Version 1.07 CERN, Geneva (1989).

[22] M.-J. Wang, Ph. D. Thesis, Case Western Reserve University, 1991 (unpublished).

[23] M. J. Leitch *et al.*, Nucl. Phys. **A544**, 197c (1992); M. J. Leitch *et al.*, to appear in Phys. Rev. D.

[24] D. M. Alde *et al.*, Phys. Rev. Lett. **66**, 2285 (1991).

[25] M. J. Leitch *et al.*, Phys. Rev. Lett. **72**, 2542 (1994).

Appendix A:
SCALERS DEFINED IN THE EXPERIMENT

For completeness I include the table with the name of the scalers defined in the experiment. The names are taken from the Fortran program created to generate the ntuple file.

Description	Scaler Labels in the Ntuple file			
Basic Experim. Rates	*SEM3*	*TFI*	*TGO*	*TAPS*
Live Time	*SEM3SB*	*TFISB*	*WMONSB*	*AMONSB*
Beam Monitors	*SEM4*	*LAM4*	*WMON*	*AMON*
TFI Components	s34muLR1	s34muL	s34muR	*ETFIRF*
TFI Components	*TDCCAL*	*CALIB1*	*COMPTFI*	*PULSER*
DC Logic Bus (Y matr.)	*MUL*	*MDL*	*MUR*	*MDR*
DC Logic Bus (mu PS)	s34muRPS	eMu	s34muLR2	*TGIDB*
DC Logic Bus (Calor.)	Cal	*ee*	s24M	Dihad
DC Logic Bus (Splash)	*X4LX4R*	*DIMU*	*NX1*	*NX3*
TGO triggers	DihadSB	*LIKESB*	s24MSB	
TGO triggers	*SINKSB*	SudMuMu	*CALIB2*	*SUSD16*
1st RF buckets monitor	*X3L7*	*Y1R3*	*X3L7Y1R3*	ditto
2nd RF buckets monitor	*RFEARLY*	*RFIN*	*RFLATE*	*TARGET*
other diagn. DT monitr.	*AMONDCB*	*LIKE*	*RFCLKPS*	*RFBCKPS*
mu- rates	*X4L*	*X4R*	*Y4L*	*Y4R*
Magnet currents	*ME6COM*	*SM12AI*	*SM3AI*	
ECL cable (rate studies)	*ECL1*	*ECL2*	*ECL3*	*ECL4*
ECL cable (rate studies)	*ECL5*	*ECL6*	*ECL7*	*ECL8*

Description	Scaler Labels in the Ntuple file			
ECL cable (rate studies)	*ECL9*	*ECL10*	*ECL11*	*ECL12*
ECL cable (rate studies)	*ECL13*	*ECL14*	*ECL15*	*ECL16*
TFI Components	s34LR	s34L	s34R	*s24CAL*
in/out time etc.	*INTIME*	*OUTTIME*	*AMONTPB*	s34MR
	INOUTIM	*AMONSEM*	*TAPSTGO*	*TAPSSEM*
	RFINEAR	*RFLAEAR*	*TGOSEM*	s34MULR3
MISC NTP	*RUN*	*SPILL*	*YEAR*	*DAY*
MISC NTP	*HOUR*	*ABSPILL*		

Appendix B:
RUN NUMBERS

Run numbers with the number of spills in the run, the beginning and end value of the spill, and the location of the run in the tape are included. Although run 446 is duplicated in the data analysis tape they are different runs.

RUN	Number of Spills	Spills start at	Spills end at	RUN position on tape
263	40	1	40	1
265	87	41	127	2
266	19	128	146	3
267	32	147	178	4
269	45	179	223	5
269	217	224	440	6
270	131	441	571	7
271	13	572	584	8
272	161	585	745	9
273	125	746	870	10
274	50	871	920	11
275	14	921	934	12
276	15	935	949	13
277	103	950	1052	14
278	42	1053	1094	15
279	42	1095	1136	16
280	4	1137	1140	17
281	5	1141	1145	18
282	5	1146	1150	19
283	5	1151	1155	20
284	7	1156	1162	21
285	6	1163	1168	22
286	4	1169	1172	23
287	5	1173	1177	24

RUN	Number of Spills	Spills start at	Spills end at	RUN position on tape
288	4	1178	1181	25
289	4	1182	1185	26
290	4	1186	1189	27
291	17	1190	1206	28
292	4	1207	1210	29
293	5	1211	1215	30
294	4	1216	1219	31
295	5	1220	1224	32
296	7	1225	1231	33
297	3	1232	1234	34
298	5	1235	1239	35
299	4	1240	1243	36
300	6	1244	1249	37
301	1	1250	1250	38
302	1	1251	1251	39
303	4	1252	1255	40
304	3	1256	1258	41
305	9	1259	1267	42
306	55	1268	1322	43
307	35	1323	1357	44
308	6	1358	1363	45
309	82	1364	1445	46
310	130	1446	1575	47
312	11	1576	1586	48
313	200	1587	1786	49
314	47	1787	1833	50
315	55	1834	1888	51
316	80	1889	1968	52
317	111	1969	2079	53
318	66	2080	2145	54
319	82	2146	2227	55
320	70	2228	2297	56
324	79	2298	2376	57
329	42	2377	2418	58
330	113	2419	2531	59
331	22	2532	2553	60
334	119	5656	5774	125
335	129	2554	2682	61

RUN	Number of Spills	Spills start at	Spills end at	RUN position on tape
336	3	2683	2685	62
337	1	2686	2686	63
345	1	2687	2687	64
350	8	5775	5782	126
351	39	5783	5821	127
352	191	5822	6012	128
353	15	2688	2702	65
366	30	2703	2732	66
367	42	2733	2774	67
368	50	2775	2824	68
369	27	2825	2851	69
370	105	2852	2956	70
371	101	2957	3057	71
372	8	3058	3065	72
373	11	3066	3076	73
374	191	3077	3267	74
375	184	3268	3451	75
376	25	3452	3476	76
377	24	3477	3500	77
378	5	3501	3505	78
379	33	3506	3538	79
382	25	3539	3563	80
383	5	3564	3568	81
384	86	3569	3654	82
386	24	3655	3678	83
387	67	3679	3745	84
389	77	6013	6089	129
391	61	6090	6150	130
392	108	6151	6258	131
393	26	6259	6284	132
394	91	6285	6375	133
395	78	3746	3823	85
396	18	3824	3841	86
397	147	3842	3988	87
398	120	3989	4108	88
399	100	4109	4208	89
400	34	6376	6409	134
401	43	6410	6452	135

RUN	Number of Spills	Spills start at	Spills end at	RUN position on tape
402	66	6453	6518	136
403	55	6519	6573	137
404	61	6574	6634	138
405	78	6635	6712	139
406	83	6713	6795	140
407	61	6796	6856	141
408	91	6857	6947	142
409	103	6948	7050	143
410	64	7051	7114	144
411	29	7115	7143	145
412	50	7144	7193	146
413	35	7194	7228	147
415	41	7229	7269	148
416	94	7270	7363	149
417	61	7364	7424	150
418	43	7425	7467	151
419	52	7468	7519	152
420	46	7520	7565	153
421	77	7566	7642	154
422	81	7643	7723	155
423	10	7724	7733	156
430	37	4209	4245	90
431	9	4246	4254	91
432	4	4255	4258	92
433	10	4259	4268	93
434	18	4269	4286	94
435	45	4287	4331	95
437	36	4332	4367	96
438	7	4368	4374	97
439	27	4375	4401	98
442	50	4402	4451	99
443	32	4452	4483	100
445	44	4484	4527	101
446	29	4528	4556	102
446	39	4557	4595	103
447	79	4596	4674	104
448	9	4675	4683	105
449	42	4684	4725	106
450	26	4726	4751	107
451	3	4752	4754	108

RUN	Number of Spills	Spills start at	Spills end at	RUN position on tape
452	85	4755	4839	109
453	21	4840	4860	110
454	30	4861	4890	111
457	36	4891	4926	112
458	58	4927	4984	113
459	20	4985	5004	114
460	53	5005	5057	115
461	38	5058	5095	116
462	160	5096	5255	117
463	87	5256	5342	118
466	66	5343	5408	119
541	20	5409	5428	120
542	11	5429	5439	121
543	17	5440	5456	122
544	18	5457	5474	123
549	181	5475	5655	124

Appendix C:
TARGET ASSIGNMENT

I divided *ME6COM* and *TARGET* values in four regions corresponding to the four targets. The lower and upper values of the target scalers for the each target are given in Table C:.1. Using the above cuts as target definition I looked for discrepancies between *TARGET* and *ME6COM* scalers. In those spills where the target scalers disagreed I looked at the value of the *Y1R3/SEM3*. Results of the study of the target selection are shown in Table C:.2.

Table C:.1: Definition of Target cuts. Cuts on *TARGET* and *ME6COM* scalers defined to select the targets of the experiment.

	TARGET/10000		*ME6COM*	
	lower	upper	lower	upper
Target 1	0	20	0	120
Target 2	20	48	200	350
Target 3	48	75	450	600
Target 4	75	-	670	-

Table C:.2: Spills where *TARGET* and *ME6COM* scalers disagreed and *Y1R3/SEM3* could give some information about the target that was in the beam.

RUN	SPILLS		Targets		
	run	absolute	*TARGET*	*ME6COM*	*Y1R3/SEM3*
351	33	5815	4	1	4
	35	5817	2	1	2
	36	5818	3	1	unknown
371	33	2989	2	3	3
373	2	3067	1	3	2
	3	3068	1	2	2
	4	3069	1	3	3
	5	3070	1	4	4
	7	3072	1	2	2
	8	3073	1	3	3
	9	3074	1	4	4
376	8	3459	3	1	3
	15	3466	1	2	2
	16	3467	2	3	3
	17	3468	2	4	4
	23	3474	1	2	2
	25	3476	2	4	4
389	62	6074	3	4	4
391	8	6097	3	4	3
	11	6100	2	3	3
	12	6101	3	4	4
	26	6115	2	3	3
395	53	3798	1	2	2
	54	3799	2	3	3
	55	3800	3	4	4
	56	3801	1	2	2
397	41	3882	3	1	3
400	31	6406	3	4	unknown
	33	6408	3	2	unknown
	34	6409	3	4	unknown

(continued on following page)

Table C:.2 (continued)

RUN	SPILLS		Targets		
	run	absolute	*TARGET*	*ME6COM*	*Y1R3/SEM3*
402	42	6494	3	4	3
403	42	6560	1	2	2
406	80	6792	3	4	4
410	42	7092	3	4	4
	46	7096	3	4	4
	54	7104	3	4	4
418	13	7437	2	3	3
	14	7438	3	4	4
421	3	7568	2	1	2
422	31	4362	3	1	unknown
437	30	4361	1	2	2
	33	4364	1	2	2
	34	4365	1	3	3
	35	4366	1	2	2
	36	4367	1	3	3
442	48	4449	3	4	4
443	24	4475	1	2	2
445	37	4520	2	1	2
452	33	4787	4	1	4
	36	4790	3	1	3
549	56	5530	3	2	unknown